INSTITUTE OF ELECTRONIC MATERIALS TECHNOLOGY

MATERIAŁY ELEKTRONICZNE

ELECTRONIC MATERIALS

QUARTERLY

Vol. 44, No. 4
2016

Creating the English language version of the journal „Electronic Materials" and digitalization of „Electronic Materials" to provide and maintain open access through the Internet - tasks financed in accordance with the 593/P-DUN/2017 agreement from the funds of the Ministry of Science and Higher Education intendend for the science dissemination fund.

WARSAW ITME 2016

MATERIAŁY ELEKTRONICZNE
ELECTRONIC MATERIALS

Vol. 44 No. 4 2016

CONTENTS

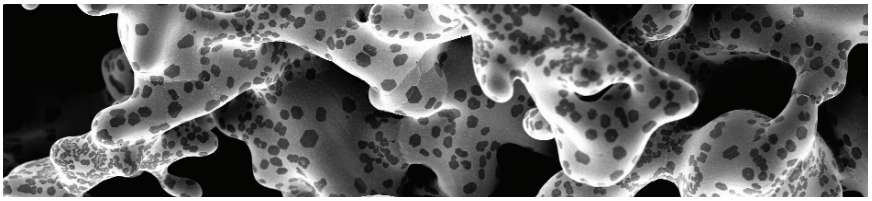

On the cover:
Copper powder covered with graphene domains.

Author of the photo - Iwona Jóźwik.
Sample from Iwona Pasternak.

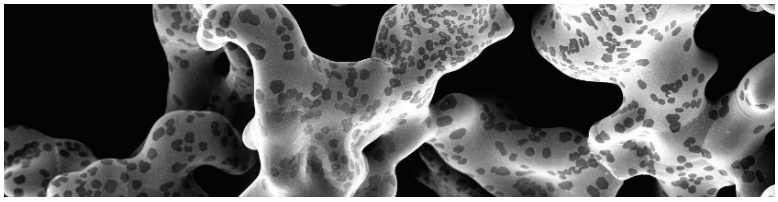

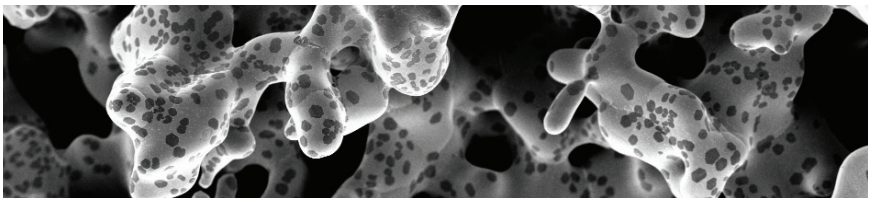

EDITORIAL OFFICE ADDRESS

Institute of Electronic Materials Technology
Wólczyńska Str. 133, 01-919 Warsaw
e-mail: ointe@itme.edu.pl
www: matelektron.itme.edu.pl

CONTACT

Associate Editor phone: (22) 639 58 85
Editorial Assistant phone: (22) 639 55 29

PL ISSN 0209 - 0058

A quarterly quoted on the list of scientific journals of the Ministry of Science and Higher Education
7 points - according to the statement of the Ministry of Science and Higher Education.

Published articles are indexed in databases:
BazTech, CAS - Chemical Abstracts and Index Copernicus

Published articles of a scientific nature are reviewed by independent researchers.

The paper version is the primary version.

The quarterly is published in open access.

Circulation: 200 copies

Viscosity sensor with shear-horizontal acoustic plate mode on BT-cut quartz and surface acoustic wave filter for mode selection

Waldemar Soluch[1], Tadeusz Wróbel[1]

Shear horizontal acoustic plate mode (SHAPM) liquid viscosity sensor with the surface acoustic wave (SAW) filter for a chosen SHAPM selection was developed. A turnover temperature and a quadratic temperature coefficient of frequency of about 0°C and −25 ppb/(°C)^2, respectively, were obtained for a delay line on BT-cut quartz (−50.5°YX90°), with gold electrodes. An acoustically coupled resonator filter for a SHAPM selection was designed and fabricatedon the 38°YX cut quartz. With inductive coils of about 0.5 μH connected in series with a 50 Ω load, the measured IL of about 2 dB at a center frequency of about 100.4 MHz was obtained for the filter. For a SHAPM delay line with the filter, insertion loss, turnover temperature, and quadratic temperature coefficient of frequency of about 12 dB, 5°C, and −30 ppb/(°C)^2, respectively, were obtained. Insertion loss and frequency changes against product of mass density and viscosity were measured, using water and glycerin solutions. Insertion loss, and frequency changes of about 14 dB, and −18 kHz, respectively, were obtained, in a viscosity range from about 1 mPa·s to 1000 mPa·s.

Key words: quartz, acoustic plate modes, surface acoustic wave, delay line, resonator filter, viscosity sensor

Czujnik lepkości z poprzecznym akustycznym modem płytowym na kwarcu BT i filtrem z akustyczną falą powierzchniową do selekcji modu

Opracowano czujnik lepkości cieczy na poprzecznym horyzontalnym akustycznym modzie płytowym (PHAMP) z filtrem na akustycznej fali powierzchniowej (AFP) do selekcji wybranego modu. Dla linii opóźniającej na kwarcu o orientacji BT (−50,5°YX90°) ze złotymi elektrodami uzyskano paraboliczną zależność zmian częstotliwości w funkcji temperatury. Punkt zwrotny paraboli wystąpił dla temperatury około 0°C a współczynnik temperaturowy wyniósł około −25 ppb/(°C)^2. Filtr rezonatorowy z AFP zaprojektowano i wykonano na kwarcu o orientacji 38°YX. Z cewkami o indukcyjności około 0,5 μH, połączonymi seryjnie z obciążeniem 50 Ω, uzyskano tłumienność wtrącenia około 2 dB na częstotliwości 100,4 MHz. Dla linii opóźniającej połączonej kaskadowo z filtrem, uzyskano tłumienność wtrącenia około 12 dB, punkt zwrotny paraboli wystąpił w temperaturze 5°C, a współczynnik temperaturowy wyniósł około −30 ppb/(°C)^2. Do pomiaru zmian tłumienności wtrącenia i częstotliwości w funkcji iloczynu gęstości masy i lepkości dynamicznej zastosowano wodne roztwory gliceryny. W zakresie lepkości od 1 mPa·s do 1000 mPa·s, uzyskano zmianę tłumienności wtrącenia o 14 dB i częstotliwości o −18 kHz.

Słowa kluczowe: kwarc, akustyczne mody płytowe, akustyczna fala powierzchniowa, linia opóźniająca, filtr rezonatorowy, czujnik lepkości

1. Introduction

Shear horizontal acoustic plate modes (SHAPMs) in BT-cut quartz are attractive for the application in viscosity sensors [1]. However, for the application in an oscillating system, a low loss and narrow bandwidth filter should be used to sufficiently attenuate both the surface transverse wave (STW) and the other SHAPMs. Because SHAPMs in BT-cut quartz are temperature compensated, the filter should also possess a similar property. The surface acoustic wave (SAW) in-line acoustically coupled resonator filter [2] with aluminum electrodes [3] on Y rotated cut of quartz [4] was therefore chosen for this application. This paper presents calculations and measurements of such filter and properties of a viscosity sensor.

2. SHAPM delay line with gold electrodes

It was previously shown that an insertion loss of about 10 dB at a frequency of about 100.4 MHz was obtained [1] for a sufficiently thick aluminum layer (0.6 μm), and after compensation of static capacitances of long interdigital transducers (IDTs) of a delay line by means of inductors (60 nH). As gold electrodes are more reliable for the operation of a viscosity sensor, in this work, the structure of the delay line with a gold layer thickness of about 0.2 μm was deposited on the delay line plane of a quartz plate, whereas the opposite sensing plane was covered with a 0.1 μm thick continues gold layer (Fig. 1).

Measured spectrum of SHAPMs and amplitude response of the chosen mode are presented in Fig. 2

[1] *Institute of Electronic Materials Technology*, 133 Wólczynska Str., 01-919 Warsaw, Poland, e-mail: w.soluch@op.pl

and 3, respectively. Compared to aluminum electrodes [1], a turnover temperature and a quadratic temperature coefficient of frequency of the chosen SHAPM are now about 0°C and −25 ppb/(°C)^2, respectively.

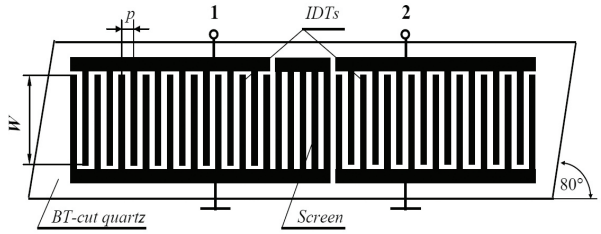

Fig. 1. Structure of the delay line.
Rys. 1. Struktura linii opóźniającej.

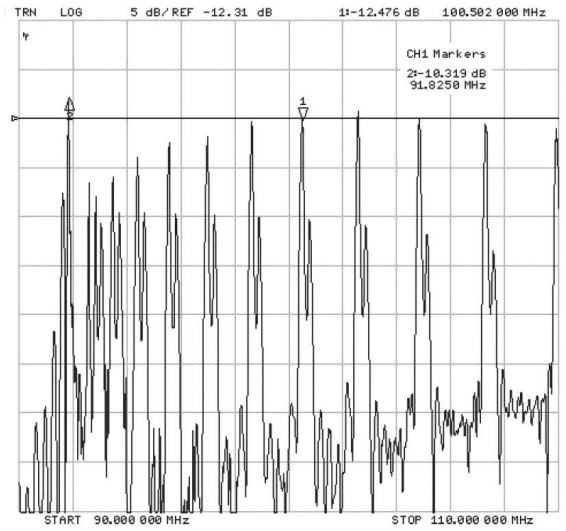

Fig. 2. Amplitude spectrum in the air.
Rys.2. Widmo amplitudowe w powietrzu.

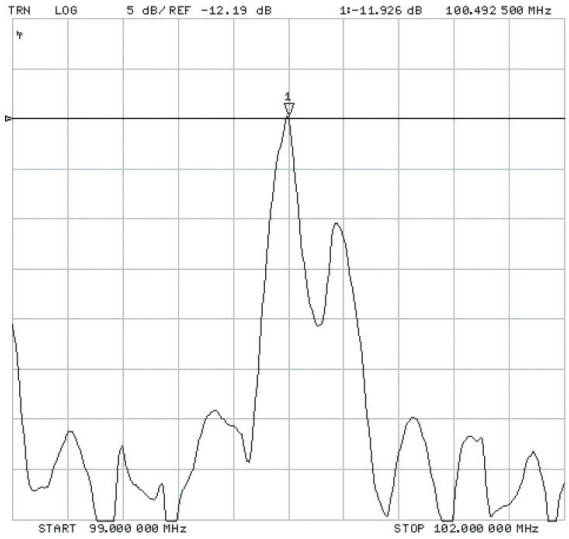

Fig. 3. Amplitude response of the chosen mode.
Rys. 3. Charakterystyka amplitudowa wybranego modu.

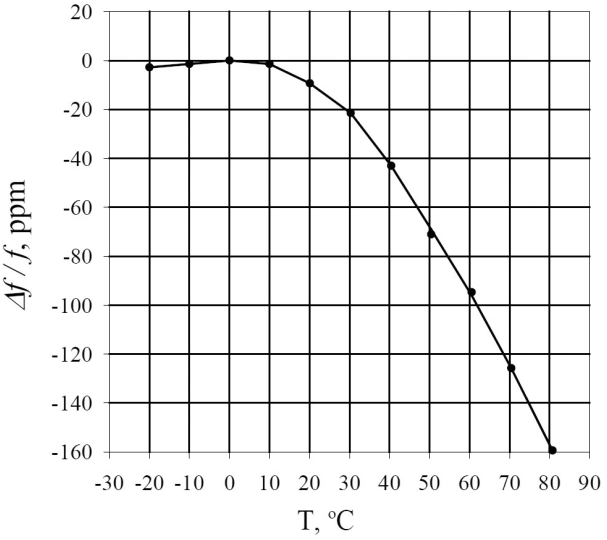

Fig. 4. Relative changes of frequency against temperature for gold electrodes.
Rys. 4. Względne zmiany częstotliwości w funkcji temperatury dla złotych elektrod.

3. Calculations and measurements of SAW filter

The SAW symmetrical in-line acoustically coupled resonator filter consists of two IDTs, one center and two end reflectors (Fig. 5) [2]. The IDTs are apodized to eliminate SAW transverse modes. Here W is the aperture, p_1 and p_2 are the electrode periods of the reflectors and the IDTs, respectively, and l is the distance between the center of the IDT electrode and the edge of the reflector electrode. The edges of quartz substrate were cut at an angle of 80° to scatter SAW propagating outside the reflectors.

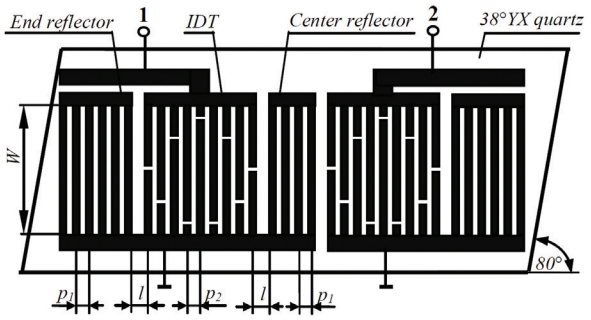

Fig. 5. Structure of symmetrical acoustically coupled resonator filter.
Rys. 5. Struktura symetrycznego filtru rezonatorowego ze sprzężeniem akustycznym.

The transfer function A_{12} of the filter can be written as [2]:

$$A_{12} = \frac{G_{12}P_0^2}{(P_1 - G_{11}P_2)^2 - (G_{12}P_2)^2}, \qquad (1)$$

$$P_0 = tS_{13}[1 + r\,(S_{12} - S_{11})], \tag{2}$$

$$P_1 = 1 - rS_{11}, \tag{3}$$

$$P_2 = t^2\,[r\,(S_{12}^2 - S_{11}^2) + S_{11}], \tag{4}$$

$$t = T_i \exp(-j\Theta), \tag{5}$$

$$r = \Gamma \exp(-j2\Theta), \tag{6}$$

$$\Theta = \omega\left(\frac{1}{v_f} + \frac{(N_t - 1)\,p_2/2}{v_t}\right). \tag{7}$$

S_{ij} (i, j = 1, 2, 3) are the scattering coefficients of the IDT [2]; G_{kl} (k, l = 1, 2) are the scattering coefficients of the center reflector; T_i is the loss coefficient; Γ is the reflection coefficient of the end reflector; v_f is the free surface SAW velocity; v_t is the SAW velocity in the areas of the IDTs and the reflectors and N_t is the number of the IDT electrodes.

Admittance of an apodized IDT with internal reflections, required for determination of S_{ij}, can be determined by the multichannel method [5]. In this method, the IDT is divided into sufficient number of channels which are connected in parallel. Admittance of each channel is calculated from an analytical expression presented in [6 − 7].

Insertion losses IL of the filter can be calculated from the expression

$$IL = -20 \log |A_{12}| \tag{8}$$

This filter should possess low insertion loss at a frequency of the chosen mode, it should suppress the other modes, and it should be fabricated on a temperature compensated substrate.

Taking into account the effect of the turnover temperature changes caused by the aluminum layer [3], the 38°YX cut quartz was chosen for the filter [4]. The following data of SAW on this cut were used for the design of the filter: v_f = 3154 m/s, v_t = 3136 m/s, K_2 = 0.125% [4], $\gamma = -0.62\,h/\lambda$, where v_f, K_2, γ, h and λ and are the free surface velocity, square of the electromechanical coupling coefficient, reflection coefficient of a single strip of the IDT, thickness of the aluminum layer and SAW wavelength, respectively. It was found that, aluminum layer thickness of about 0.6 μm should be used to obtain sufficient bandwidth of the filter. The following data were obtained for the final structure of the designed filter: W = 2.5 mm, p_1 = 15.57 μm, p_2 = 15.45 μm, N_t = 101, N_e = 250 and N_c = 10, where N_t, N_e and N_c are the number of electrodes of the IDT, the end and the center reflectors, respectively. The loss coefficient T_i = 1 (no losses) was used for the design.

The filter was fabricated by the lift-off method, mounted in metal packages and measured (using Agilent Network Analyzer Type 8753ET, Santa Rosa, CA). The measured and calculated amplitude responses with inductive coils of about 0.5 μH connected in series with the 50 Ω load, are shown in Fig. 6. The measured IL of about 2 dB at a center frequency of about 100.4 MHz was obtained. To obtain the same reference level as the one received in the measurement necessitated, the use of the loss coefficient T_i = 0.954 in the calculation.

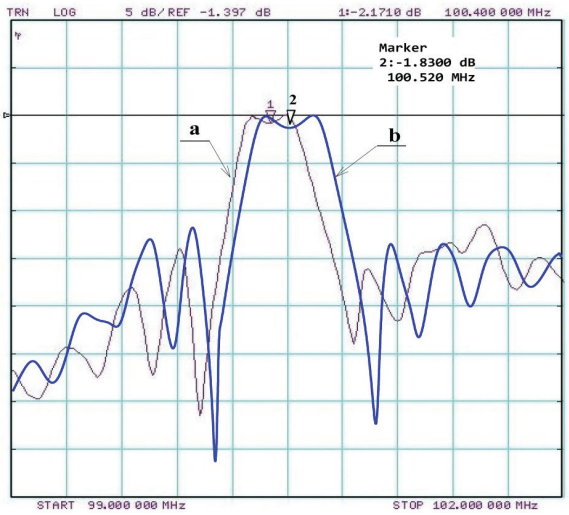

Fig. 6. Measured (a) and calculated (b) amplitude responses of the filter.
Rys. 6. Zmierzona (a) i obliczona (b) charakterystyki amplitudowe filtru.

4. Properties of viscosity sensor

The SHAPM delay line and SAW filter with matching inductors were connected in cascade (Fig. 7) and measured in the air (Fig. 8 − 9). All other modes were attenuated by more than 20 dB with respect to the chosen mode. For the SHAPM delay line with the filter we obtained, insertion loss, turnover temperature, and quadratic temperature coefficient of frequency of about 12 dB, 5°C, and −30 ppb/(°C)^2 in the air, respectively.

Insertion loss ΔL and frequency changes Δf against $\sqrt{\rho\eta}$, where ρ [g/cm^3] and η [mPa·s] are the mass density and viscosity of glycerin and water solutions, respectively and are shown in Fig. 10. In a viscosity range from about 1 mPa·s to 1000 mPa·s, the obtained insertion loss and frequency changes were about 14 dB, and −18 kHz, respectively.

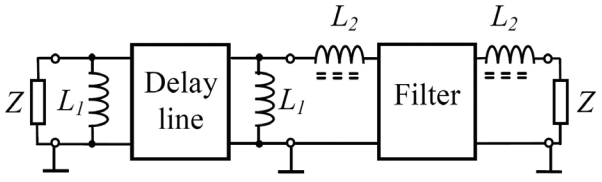

Z = 50 Ω, L_1 = 60 nH, L_2 = 0.5 μH

Fig. 7. Delay line and filter with matching inductors.
Rys. 7. Linia opóźniająca i filtr z cewkami dopasowującymi.

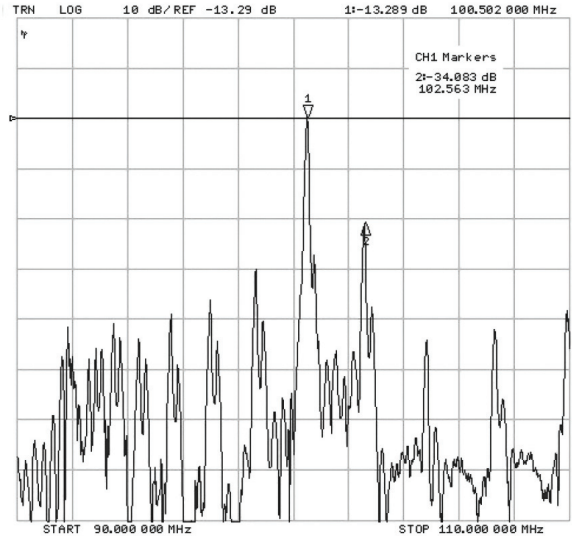

Fig. 8. Amplitude response of sensor with filter.
Rys. 8. Charakterystyka amplitudowa czujnika z filtrem.

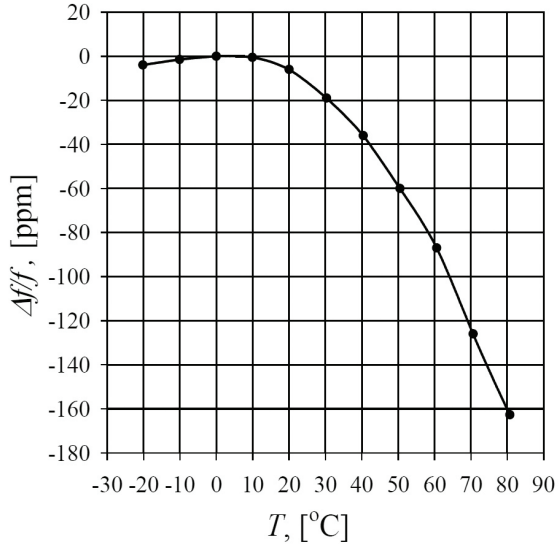

Fig. 9. Relative frequency changes against temperature.
Rys. 9. Względne zmiany częstotliwości w funkcji temperatury.

5. Conclusions

SHAPM viscosity sensor with SAW filter was developed. A turnover temperature and a quadratic temperature coefficient of frequency of about 0°C and −25 ppb/(°C)^2, respectively, were obtained for a delay line on BT-cut quartz (−50.5°YX90°) with gold electrodes. The SAW in-line acoustically coupled resonator filter for the SHAPM selection in BT-cut quartz was designed and fabricated on the 38°YX cut quartz. For the SHAPM delay line with the filter, insertion loss, turnover temperature, and quadratic temperature coefficient of frequency of about 12 dB, 5°C, and −30 ppb/(°C)^2 in air, respectively, were obtained. Using water and glycerin solutions, insertion loss and frequency changes against product of mass density and viscosity.

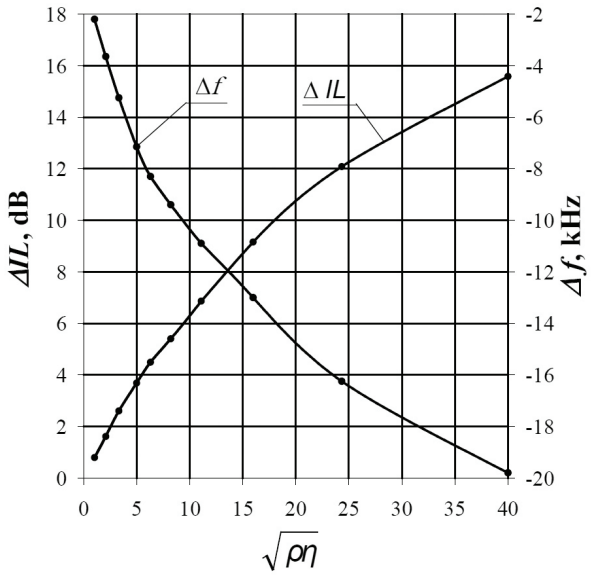

Fig. 10. Insertion loss (Δ*IL*) and frequency (Δ*f*) changes against $\sqrt{\rho\eta}$.
Rys. 10. Zmiany tłumienności wtrącenia (Δ*IL*) i częstotliwości (Δ*f*) w funkcji $\sqrt{\rho\eta}$.

In a viscosity range from about 1 mPa·s to 1000 mPa·s, insertion loss and frequency changes of about 14 dB, and −18 kHz, respectively, were obtained.

Acknowledgement

The authors would like to thank Marianna Baranowska for her assistance in making the drawings for this paper.

References

[1] Soluch W., Lysakowska M.: Properties of shear horizontal acoustic plate modes in BT-cut quartz, *IEEE Trans., Ultrason. Ferroelectr. Freq. Control*, 2011, 58, 2239 − 2243

[2] Rosenberg R. L., Coldren L. A.: Scattering analysis and design of SAW resonator filters, *IEEE Trans. Sonics and Ultrason.*, 1979, SU−26, 205 − 225

[3] Shimizu Y., Terazaki A., Sakaue T.: *Temperature dependence of SAW velocity for metal film on a-quartz*, *Proc. IEEE Ultrason. Symp*. 1976, 519 − 522

[4] Parker T. E., Montress G. K.: Precision surface wave (SAW) oscillators, *IEEE Trans., Ultrason. Ferroelectr. Freq. Control*, 1988, 35, 342 − 364

[5] Tancrell R. H., Holland M. G.: Acoustic surface wave filters, *Proc. IEEE*, 1971, 59, 393 − 409

[6] Koyamada Y., Yoshikawa S.: Coupled mode analysis of a long IDT, *Rev. Electr. Commun. Lab. (Jpn.)*, 1979, 27, 432 − 444

[7] Soluch W.: Scattering matrix approach to STW resonators, *IEEE Trans. Ultrason., Ferroelect., Freq. Contr.*, 2002, 49, 327 − 330

Mechanical strength and fracture toughness of brittle monocrystalline and ceramic materials

Marek Boniecki[1], Paweł Kamiński[1], Władysław Wesołowski[1], Konrad Krzyżak[1]

The article compares the mechanical properties of a n-type silicon single crystal with an orientation <100> and resistivity ~ 2000 Ωcm, obtained by the floating zone (FZ) method, with the mechanical properties of Y_2O_3 ceramics. Both materials are characterized by a high value of transmission coefficient of electromagnetic radiation in the wavelength range from 2 μm to 8 μm and they can be used as optical windows in a near infrared range. However, the choice of a material type for the specific applications may depend on their mechanical properties. These properties have been determined both at room temperature and at elevated temperature, i.e. 700°C for Si and 800°C for Y_2O_3 ceramics. We have found that at room temperature the fracture toughness of the Si single crystal K_{Ic} = 1.3 ± 0.1 MPam$^{1/2}$ and the four-point bending strength σ_c = 289 ± 61 MPa. For Y_2O_3 ceramics these parameters are 1.8 ± 0.2 MPam$^{1/2}$ and 184 ± 20 MPa, respectively. At 700°C the mechanical parameters for the Si single crystal are: K_{Ic} = 20 ± 3 MPam$^{1/2}$ and σ_c = 592 ± 86 MPa. For Y_2O_3 ceramics at 800°C, K_{Ic} = 1.7 ± 0.1 MPam$^{1/2}$ and σ_c = 230 ± 23 MPa. The presented data show that at elevated temperatures both fracture toughness and bending strength of the Si single crystal are significantly greater than the values of those parameters found for Y_2O_3 ceramics.

Key words: Y_2O_3 ceramics, high-purity silicon, fracture toughness, bending strength

Wytrzymałość mechaniczna i odporność na pękanie kruchych materiałów monokrystalicznych i ceramicznych

W artykule porównano właściwości mechaniczne monokrystalicznego krzemu typu n o orientacji <100> i rezystywności ~ 2000 Ωcm, otrzymanego metodą beztyglową, z właściwościami mechanicznymi ceramiki Y_2O_3. Oba materiały charakteryzują się dużym współczynnikiem transmisji promieniowania elektromagnetycznego w zakresie długości fali od 2 μm do 8 μm i mogą być stosowane jako okna optyczne w zakresie bliskiej podczerwieni. Wybór rodzaju materiału dla konkretnych zastosowań może być jednak uzależniony od ich właściwości mechanicznych. Właściwości te określano zarówno w temperaturze pokojowej, jak i w temperaturze podwyższonej do 700°C w przypadku Si oraz do 800°C w przypadku ceramiki Y_2O_3. Stwierdzono, że dla Si w temperaturze pokojowej odporność na pękanie K_{Ic} = 1,3 ± 0,1 MPam$^{1/2}$,a wytrzymałość na zginanie czteropunktowe σ_c = 289 ± 61 MPa. Dla Y_2O_3 parametry K_{Ic} i σ_c przyjmują wartości wynoszące w tej temperaturze odpowiednio 1,8 ± 0,2 MPam$^{1/2}$ i 184 ± 20 MPa. W temperaturze 700°C wartości parametrów K_{Ic} i σ_c dla Si są równe odpowiednio 20 ± 3 MPam$^{1/2}$ oraz 592 ± 86 MPa, zaś dla ceramiki Y_2O_3 w 800°C K_{Ic} = 1,7 ± 0,1MPam$^{1/2}$ i σ_c = 230 ± 23 MPa. Prezentowane dane wskazują, że w temperaturze pokojowej wytrzymałość na zginanie czteropunktowe monokrystalicznego Si jest znacząco większa niż ceramiki Y_2O_3. W podwyższonych temperaturach zarówno odporność na pękanie, jak i wytrzymałość na zginanie monokrystalicznego Si jest wielokrotnie większa niż w przypadku ceramiki Y_2O_3.

Słowa kluczowe: ceramika Y_2O_3, krzem, odporność na pękanie, wytrzymałość na zginanie

1. Introduction

Polycrystalline ceramic materials and single crystals of semiconductors are characterized by brittle cracking. It occurs at a minimal plastic deformation, which leads to an immediate destruction of the material. This cracking usually starts from the defects already present in the material and disturb its structure. The defects can exist on the surface or in the bulk of the material. Molecules or atoms of a solid are bound together by the cohesive forces originating from the chemical or physical interactions. The cohesive strength of a material is its maximum strength, which is determined by the strength of the chemical bonds and which can be theoretically estimated. In practice, such strength is rarely measured because of the aforementioned presence of numerous structural defects in the material. These defects may be microcracks, pores, inclusions of foreign phases, etc. If a load is applied to a sample made from a material containing defects, the stress concentration at the edges of these becomes many times bigger than the stress value resulting from the applied force in the defect free material. Stress concentration exeeding the material cohesive strength, result in the appearanace of a crack. The cracking criterion is determined by the state of the stress field near the edges of the existing defect.

[1] *Institute of Electronic Materials Technology*, 133 Wólczynska Str., 01-919 Warsaw, Poland, e-mail: Marek.Boniecki@itme.edu.pl

The stress field is related to the shape and the size of the defect (usually understood as a crack that disturbs the continuity of the material structure) as well as to the type and the magnitude of the applied load. The analysis of that problem can be found in many textbooks and articles [1 - 4]. It presents the concept of stress intensity factor K, is proportional to the value of the applied load and depends also on the load type and the microcrack geometry. The load which is intended to destroy the material can be applied in three different ways [1, 3]. One way is called *opening* and it is a displacement perpendicular to the crack surface, while the other two (*edge slip* and *tear*) are associated with a shift parallel to the crack edge. For brittle materials (weak for stretching) the most important is the *opening* way.

It has been accepted in the literature to denote stress intensity factor corresponding to the sample destruction as K_I, which is expressed as:

$$K_I = \sigma Y \sqrt{c}, \tag{1}$$

where: σ is the applied stress, Y is a constant dependent on the geometry of the sample and the defect (crack), while c is the crack length.

The maximum value of this factor, for the material cracking, is marked with the symbol K_{Ic} and is called fracture toughness. The value of K_{Ic} is characteristic of a given material and thus it is used to compare the mechanical properties of different materials. The destruction of a brittle material proceeds suddenly without any visible symptoms (i.e. a noticeable plastic deformation), but it is usually preceded by subcritical cracks growth. It means that under the applied stress, smaller than the critical stress (i.e. strength of the material), the initial crack present in the material starts to lengthen, reaching the critical value c_k, at which the material breaks and $K_I = K_{Ic}$. This phenomenon is described by the equation [4]:

$$V = AK_I^n, \tag{2}$$

where: V is the propagation velocity of subcritical cracks and A and n are the parameters of the subcritical cracks growth.

The dimensions of the defects in a brittle material generated during the technological process of its production directly affect the strength σ_c of the individual samples used for the examination of their mechanical properties by a testing machine. The parameter σ_c is given by the equation:

$$\sigma_c = \frac{K_{Ic}}{Y\sqrt{c_k}}, \tag{3}$$

The samples of a material, obtained during sintering and mechanical machining, differ in respect of the size of the defect, from which the crack growth begins and further leads to the sample destruction. Therefore, the values of the strength σ_c exhibit a particular statistical distribution. Usually this is the Weibull distribution [5], although in practice it happens to be close to the normal (Gaussian) distribution [6].

With increasing temperature, the plasticity of the material increases. It may change abruptly as in the case of a silicon single crystal, for which the temperature of the transition from a brittle to plastic state ranges from ~ 545°C to ~ 645°C, depending on the deformation rate ranging from 1.3×10^{-6} s^{-1} to 2.6×10^{-5} s^{-1} [7]. This change is accompanied by a sudden increase in the strength and fracture toughness [7]. In the case of ceramic materials, the increase in plasticity occurs gradually as a function of temperature and it does not have to be accompanied by an increase in K_{Ic} and σ_c, as it takes place e.g. in the case of Al_2O_3 ceramics [8]. On the contrary, for Y_2O_3 ceramics the values of K_{Ic} and σ_c increase or remain constant with increasing the plasticity [9 -10].

The goal of this work is to present the methodology and the results of the studies on mechanical strength, fracture toughness and subcritical crack growth for a Si single crystal of a high purity, obtained by the floating zone (FZ) method, as well as to compare our data with the previously determined mechanical properties of Y_2O_3 polycrystalline ceramics. These materials, despite their diverse microstructure, are characterized by a high value of transmission coefficient of electromagnetic radiation of the wavelength ranging from 2 μm to 8 μm and can be utilized for the production of windows transmitting the radiation in a near infrared range [11 - 12]. The comparison of the mechanical properties of these materials is very important for the selection of the type of material from the viewpoint of the requirements for the specific applications.

Mechanical properties of a Si single crystal and Y_2O_3 ceramics were examined both at room temperature and at elevated temperatures. The obtained results indicate that the measurement methods based on the theory of brittle fracture mechanics can be effectively applied to study the mechanical properties of materials of a very diversified microstructure.

2. Experimental

2.1. Samples for testing

• Si single crystal samples.

Silicon wafers mirror-like polished on one side, with a diameter of 100 mm and a thickness of 0.3 mm, were used for the tests. They were made from an n-type Si single crystal of high purity, obtained by the floating zone (FZ) method. The Si single crystal was oriented in the crystallographic direction <100> and doped with phosphorus, whose concentration was ~ 3×10^{12} cm^{-3}. The resistivity of the single crystal was ~ 2000 Ωcm. The concentration of nitrogen in the single crystal was below 3×10^{14} cm^{-3},

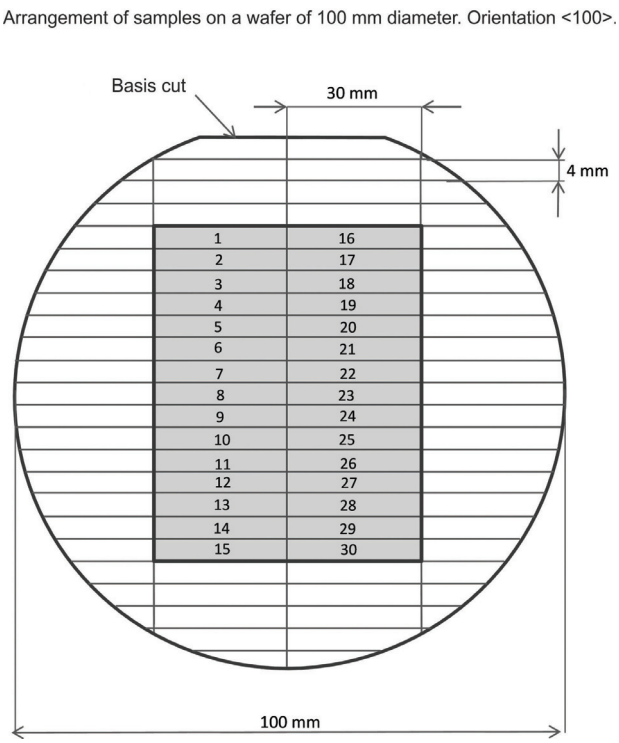

Fig. 1. Arrangement of samples on a wafer made from a high-purity Si single crystal used for the tests of mechanical properties.
Rys. 1. Układ próbek na płytce z monokryształu Si o wysokiej czystości użytych do badania właściwości mechanicznych.

the concentration of oxygen was ~ 5 × 10^{15} cm^{-3}, and the concentration of carbon was below 5 × 10^{15} cm^{-3}. The silicon wafers were cut into the samples of a 4-mm width and a 30-mm length 30 mm, according to the diagram shown in Fig. 1.

• Y_2O_3 ceramics samples.

In this paper we cite the results obtained in [13 - 14] for the samples made from Y_2O_3 ceramics. A detailed description of the preparation of the ceramic samples is given in [13]. The samples used to test their mechanical properties were characterized by a density equal to 99% of the theoretical density, i.e. 5.03 g/cm^3, and by an average grain size of 6 ± 3 μm.

2.2. Tests of mechanical properties

The mechanical properties of the Si single crystal and Y_2O_3 ceramics were tested by the determination of three- and four-point bending strength, fracture toughness and Young's modulus. Three- and four-point bending strength σ_c can be expressed in the form:

$$\sigma_c = \frac{1.5P_c(L-l)}{bw^2}, \tag{4}$$

where P_c is the fracture load, L - spacing of lower supports, l - distance of upper pressure rolls, b - sample width, and w - sample thickness.

For l = 0, the sample is subjected to the three-point bending. The fracture toughness K_{Ic} was determined in two ways:
(a) by three-point bending of the notched specimen,
(b) by measuring the length of the cracks propagating from the Vickers impression.

In the case of the method (a), the value of K_{Ic} was calculated from the formula:

$$K_{Ic} = Y\frac{1.5P_cL}{bw^2}c_k^{0.5}, \tag{5}$$

where Y is a geometrical constant calculated according to the description given in [15], c_k – the notch depth, while the remaining designations are as defined above.

For the method (b), K_{Ic} was calculated from the formula [16]:

$$K_{Ic} = 0.016\,(E/H)^{0.5}\,(P/c^{1.5}), \tag{6}$$

where E is elastic (Young's) modulus, H - Vickers hardness, P - load of the Vickers indenter, c - length of the cracks propagating from the corners of the impression.

A more detailed discussion on the ways of K_{Ic} measurements with the use of Vickers indenter can be found in [14].

The value of Young's modulus E was determined by the three-point bending method and calculated from the formula [15]:

$$E = \frac{L^2}{bw^2c}\left[\frac{L}{4w} + \frac{(1+v)w}{2L}\right], \tag{7}$$

where $C = \Delta y/\Delta P$ denotes the ratio of the increase in the sample deflection to the load increase, v is the Poisson constant, while the remaining designations are as defined above.

The hardness H was determined from the measurements of the diagonal length of the Vickers impression. The value of H was calculated from the formula:

$$H = 1.8544 \times P/(2a)^2, \tag{8}$$

where a is the half-length of the diagonal of the Vickers impression and P is the load of the Vickers indenter.

3. Results

A comparison of strength characteristics for the Si single crystal and for Y_2O_3 ceramics is presented in Fig. 2 in the form of diagrams of the two-parametric Weibull distribution. The tests were carried out at the loading head travelling speed of 1 mm/min at room temperature as well as at 700ºC for Si and 800°C for Y_2O_3. The measurements of σ_c for a Si single crystal were performed in a four-point

bending system using the samples with a thickness of 0.3 mm, shown in Fig. 1. The distance between the bottom supports was 20 mm, while between the upper supports it was 10 mm (the stretched surface was polished). In the case of Y_2O_3 ceramics, the sample width was 0.95 mm, thickness 1 mm and length 15 mm. The measurements of σ_c were performed in a three-point bending system with the distance between the supports equal to 8 mm.

The cumulative distribution function of two-parameter Weibull distribution is represented by the formula [5]:

$$P = 1 - \exp\left[-\left(\frac{\sigma_c}{\sigma_0}\right)^m\right], \tag{9}$$

where P denotes the probability of sample destruction under stress σ_c, σ_0 - the characteristic stress and m – the Weibull module (distribution shape parameter).

In the coordinate system where the values of $\ln(\sigma_c)$ are on the X-axis and the values of $\ln(\ln(1/(1-P)))$ are on the Y-axis, the experimental points should follow a straight line, on which to a point at a position i (the points are put with ascending strength values) the probability of a destruction given by the equation (10) [6] is assigned:

$$P = \frac{i - 0.5}{N}, \tag{10}$$

where N is the number of samples.

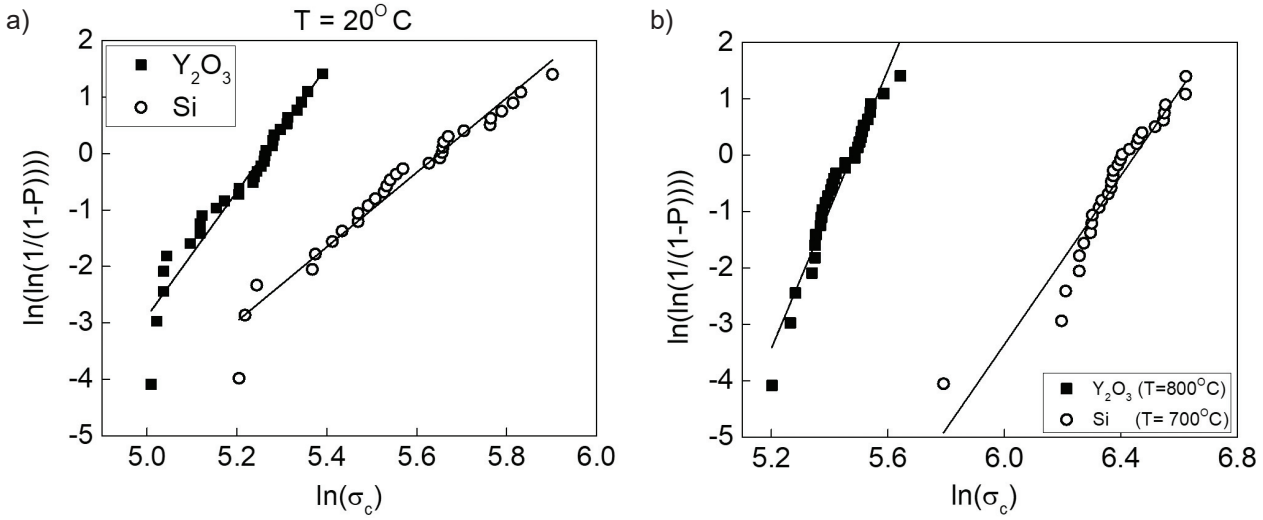

Fig. 2. Comparison of the Weibull distribution plots for the strength of the Si single crystal (wafer No. 4, Tab. 1) and Y_2O_3 ceramics: (a) at room temperature, (b) at elevated temperature (700ºC for Si and 800ºC for Y_2O_3 [13]).
Rys. 2. Porównanie wykresów rozkładu Weibulla wytrzymałości monokrystalicznego Si (płytka nr 4, Tab. 1) i ceramiki Y_2O_3: (a) w temperaturze pokojowej, (b) w temperaturze podwyższonej (700ºC dla Si i 800ºC dla Y_2O_3 [13]).

Tab. 1. Gaussian and Weibull distribution parameters of the Si wafers strength at T = 20ºC.
Tab. 1. Parametry rozkładów Gaussa i Weibulla dla wytrzymałości płytek Si w temperaturze 20ºC.

Wafer number	min (MPa)	max (MPa)	Gaussian distribution		Weibull distribution					N
			S (MPa)	O (MPa)	m	σ_o (MPa)	E_0 (MPa)	$\sigma_{0.5}$ (MPa)	W (MPa)	
1	129.7	314.5	202.0	47.5	5.08	219.2	201.2	203.9	46.5	24
2	152.1	476.3	300.2	92.0	3.73	335.7	303.0	304.3	91.1	29
3	148.3	428.3	309.5	77.5	4.34	341.8	312.0	314.1	77.8	30
4	197.1	438.8	343.7	59.8	6.44	369.4	343.5	349.0	65.5	30
Mean			**288.9**	**69.2**	**4.89**	**316.5**	**289.9**	**292.8**	**70.2**	

The symbols *min* and *max* denote the minimal and maximal measurement result respectively, N - the number of measurements. The Gaussian distribution parameters: arithmetic mean S and standard deviation O. The Weibull distribution parameters: expected value $E_0 = \sigma_u + \sigma_0\Gamma(1 + 1/m)$, variance square root $W = \sigma_0 \{\Gamma(1 + 2/m) - \Gamma^2(1 + 1/m)\}^{1/2}$, and median $\sigma_0 = \sigma_0 \ln(2)^{1/m}$ (Γ is Euler's gamma function).

Tab. 2. Gaussian and Weibull distribution parameters for the strength of Y_2O_3 ceramics at 20ºC [13].
Tab. 2. Parametry rozkładów Gaussa i Weibulla dla wytrzymałości ceramiki Y_2O_3 w temperaturze 20ºC [13].

min (MPa)	max (MPa)	Gaussian distribution		Weibull distribution					N
		S (MPa)	O (MPa)	m	σ_o (MPa)	E_0 (MPa)	$\sigma_{0.5}$ (MPa)	W (MPa)	
149.8	220.0	184.3	20	11.1	193.0	184.4	186.7	20.0	30

Tab. 3. Gaussian and Weibull distribution parameters for the strength of Si wafers and Y_2O_3 [13] ceramics at temperatures 700ºC and 800 ºC, respectively.
Tab. 3. Parametry rozkładów Gaussa i Weibulla wytrzymałości płytek Si i ceramiki Y_2O_3 [13] w temperaturach odpowiednio 700ºC i 800ºC.

Material	min (MPa)	max (MPa)	Gaussian distribution		Weibull distribution					N
			S (MPa)	O (MPa)	m	σ_o (MPa)	E_0 (MPa)	$\sigma_{0,5}$ (MPa)	W (MPa)	
Si	327.5	752.1	592.4	85.7	8.88	627.3	594.0	601.6	94.6	29
Y_2O_3	181.6	282.3	229.8	22.7	10.90	240.0	229.1	232.1	25.4	30

Tab. 1 and 2 present the calculated values of the Weibull distribution parameters derived from the plots in Fig. 2 (a) for the Si single crystal and Y_2O_3 ceramics at 20ºC, respectively. The comparison is also presented for the values of the arithmetic mean S and standard deviation O (Gaussian distribution) determined from our experimental data with the expected value E, median $\sigma_{0.5}$ and variance square root W, calculated from Weibull distribution parameters for Si and Y_2O_3 ceramics at room temperature, respectively. The strength tests of Si were carried out using the samples made from four different wafers (Tab. 1) originating from one single crystal. Tab. 3 shows the comparison of the Weibull and Gaussian distributions parameters for the Si crystal at 700ºC and Y_2O_3 ceramics at 800ºC, respectively.

Tab. 4 and 5 collect the values of K_{Ic}, E and H, determined for the Si single crystal and Y_2O_3 ceramics, respectively. Each number given in the tables is the value of an arithmetic mean for five samples.

The values of K_{Ic} and H shown in Tab. 4 were determined using the Vickers indenter at a load P = 4.9 N. The K_{Ic} values were calculated from the formula (6), while the H values was were obtained by applying the equation (8). The samples shown in Fig. 1 and the three-point bending method with a support distance of 25 mm were used to determine the Young's modulus E. The E values were determined from the formula (7), assuming ν = 0.28. It is worth adding that the fracture toughness K_{Ic} for the Si wafers determined using the notched bar samples was 1.3 ± 0.1 MPam$^{1/2}$. The measurements were carried out on the samples as shown in Fig. 1 with the notch cut in the distance of ~ 1 mm from the edge of the specimen with the support beams spacing of 20 mm.

The K_{Ic} (Vickers) and H values were determined using a Vickers indenter at a load P = 98.1 N. The E values were

Tab. 4. Fracture toughness K_{Ic}, Young's modus E and Vickers hardness H for the Sisingle crystal at room temperature 20ºC.
Tab. 4. Odporność na pękanie K_{Ic}, moduł Younga E oraz twardość Vickersa H dla monokrystalicznego krzemu w temperaturze 20ºC.

Wafer number	K_{Ic} (MPam$^{1/2}$)	E (GPa)	H (GPa)
1	0.73 ± 0.07	161 ± 14	9.9 ± 0.8
2	0.79 ± 0.06	172 ± 10	9.6
3	0.78 ± 0.08	178 ± 10	10 ± 1
4	0.70 ± 0.04	180 ± 9	9.8 ± 0.4
Mean	**0.75 ± 0.04**	**173 ± 9**	**9.9 ± 0.2**

Tab. 5. Facture toughness K_{Ic}, Young's modus E and Vickers hardness H for Y_2O_3 ceramics at 20ºC [14].
Tab. 5. Odporność na pękanie K_{Ic}, moduł Younga E oraz twardość Vickersa H dla ceramiki Y_2O_3 w temperaturze 20ºC [14].

K_{Ic} (MPam$^{1/2}$)		E (GPa)	H (GPa)
beam	Vickers		
1.8 ± 0.2	1.0 ± 0.1	158 ± 8	7.5 ± 0.2

obtained using the samples in the form of notched beams 1 mm thick, 4 mm wide and 50 mm long, by applying the three-point bending method with the support beams spacing of 40 mm. The values were calculated according to the formula (7), assuming ν = 0.3. The K_{Ic} value (beam) was determined using beam-shaped samples with a thickness of w = 4 mm, width b = 2.5 mm, length l = 30 mm,

and with the notch depth c_k = 1.1 mm, by applying the three-point bending method with the support beams spacing L = 20 mm.

It should be added that the fracture toughness K_{Ic}, measured with the use of the samples in the form of notched beams was 19.9 ± 2.6 and 1.7 ± 0.1 MPam$^{1/2}$ for the Si single crystal at 700ºC and Y_2O_3 ceramics at 800ºC, respectively [13].

When comparing the results for Si and Y_2O_3, it is necessary to comment on the reliability of the values of K_{Ic} obtained by the bending method for the notched beams, in particular for the Si wafers. In the case of the Si samples, the ratio of the transverse dimensions of the samples w/b = 4/0.3 = 13.3, while for Y_2O_3 $_{w/b}$ = 4/2.5 = 1.6. However, the formula taken from [15] and used for the calculations of K_{Ic} can be applied to all cases if the single condition $L/w \geq 2$ is fulfilled. A high w/b value for the Si samples can lead to erroneous K_{Ic} results due to a different distribution of stresses in the samples that deviate far from the standard dimensions (for w/b ranging from 1 to 4, according to an ASTM E-399-90 standard). Unfortunately, since only the 0.3 mm thick Si wafers were available to the authors, it was not technically possible to produce samples meeting the condition $1 \leq w/b \leq 4$. It should also be stressed that the notches on Si and Y_2O_3 samples were performed by the same technique (cutting up to a depth of 0.8 mm with the use of a 0.2 mm wide disc, and up to around 1 mm with the use of a 0.05 mm wide disc). The spacing between supports was 20 mm in both cases.

Among many methods of the measurement of the values of the subcritical crack growth parameters A and n (formula (2)), we have chosen the measurement of the bending strength of the beams as a function of the load application rate [17]. On the basis of the formulas (1) and (2), the following relationship has been derived in [17] between the strength σ_f for a given loading rate and the loading rate $d\sigma/dt$, expressed in the logarithmic form as:

$$\log\sigma_f = \frac{1}{n+1}\log(d\sigma/dt) + \frac{1}{n+1}\log[B(n+1)\sigma_c^{n-2}], \quad (11)$$

where: $B = 2/[(n-2)AY^2 K_{Ic}^{n-2}]$.

In the coordinate system where the values of log ($d\sigma/dt$) are on the X-axis and the values of log (σ_f) are on the Y-axis, the experimental points follow a straight line. Fig. 3 presents a comparison of the results obtained at room temperature for the Si single crystal and Y_2O_3 ceramics. The strength measurements were carried out for four displacement rates of the testing machine head: 0.001, 0.01, 0.1 and 1 mm/min. The corresponding rates of the load increase were determined on the basis of a digital recording of the force as a function of time. All the experimental points shown in Fig. 3 are averaged over 10 measurements. The parameters of the equation (11) were calculated using the least squares method, and then the values A and n (Tab. 6)

Tab. 6. Parametry równania (2) opisującego rozwój pęknięć podkrytycznych wyznaczone dla monokrystalicznego Si i ceramiki Y_2O_3.
Tab. 6. Parameters of the equation (2) describing subcritical crack growth, determined for the Si single crystal and Y_2O_3 ceramics.

Material Parameter	Si	Y_2O_3
n	75.2	51.7
A (m/s)	1.8×10^{-15}	4.8×10^{-19}

The parameters n and A for Y_2O_3 ceramics were calculated on the basis of the experimental data given in [13].

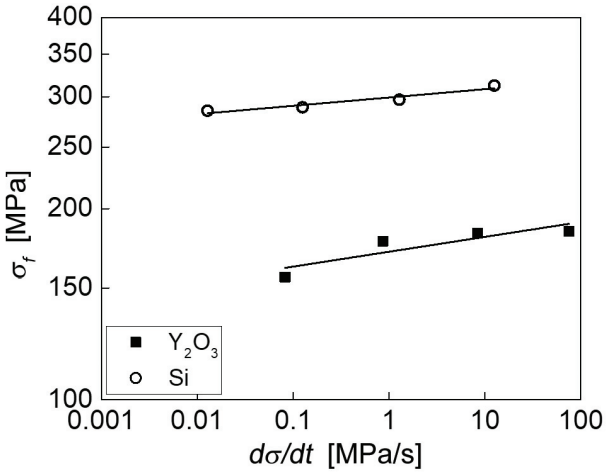

Fig. 3. Comparison of bending strength σ_f as a function of loading rate $d\sigma/dt$ for the Si single crystal and Y_2O_3 ceramics at room temperature.
Rys. 3. Porównanie wytrzymałości na zginanie σ_f w funkcji szybkości obciążania $d\sigma/dt$ dla monokrystalicznego Si i ceramiki Y_2O_3 w temperaturze pokojowej.

were obtained using the following values in the calculations σ_c and K_{Ic}: 288.9 MPa (a mean S value from Tab. 1), 184.3 MPa (S value from Tab. 2), 1.3 MPam$^{1/2}$ and 1.8 MPam$^{1/2}$ for the Si wafers and Y_2O_3 ceramics, respectively. The value of σ_c for the Si wafers corresponds to the strength measured for the load application rate of 1 mm/min, while for Y_2O_3 it is the value of parameter S from Tab. 2. The K_{Ic} values were measured on the notched beams (Tab. 4 and 5) and Y was taken from the work [3] as equal to $\sqrt{\pi}$ (1.8).

4. Discussion of the results

4.1. Comparison of mechanical properties of Si wafers and Y_2O_3 ceramics at room temperature

In the work [18], the bending strength of Si wafers (diameter ~ 76 mm and thickness 0.69 mm) was

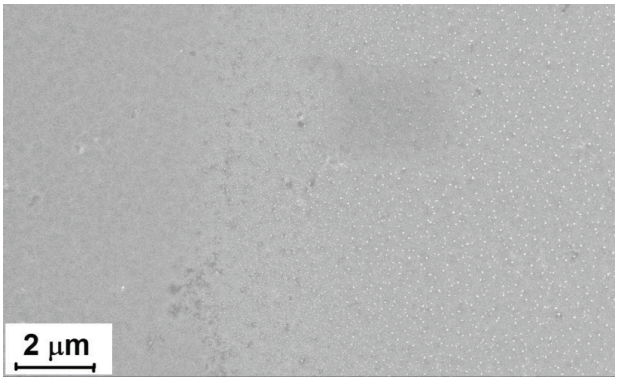

Fig. 4. Microscopic image of the etched surface of a Si wafer.
Rys. 4. Mikroskopowy obraz powierzchni płytki Si po wytrawieniu.

tested and the results depended on the method of the preparation of the wafer stretched surface. The samples originated from <111> single crystals were obtained by the FZ method. No nitrogen was detected in these samples, while the concentration of oxygen was comparable to the samples used in our study and it amounted to ~ 4×10^{15} cm^{-3}. For the Si wafers with a non-polished surface the mean strength value equalled ~ 220 MPa and the value of Weibull module m = 16.2 indicated a small scatter of the results. On the other hand, for the polished samples, the average strength value was ~ 1.1 GPa, but there was a large scatter of results (m = 3). When comparing these results with the data listed in Tab. 1, in the case of our study the observed difference can be due to a significant influence of the edge faults, which probably do not play a role in the load geometry used in [18]. This fact may signify that the mean strength of the polished Si samples in our work is slightly higher than that of the non-polished ones in [18], but at the same time the scatter of the test results is large. For Y_2O_3, the value of m = 11.1 indicates that the scatter of the results is smaller than in the case of Si wafers, even though the ceramic samples were not polished. In [19] for the non-polished Al_2O_3 ceramic samples the value of parameter m was also ~ 11 (the samples were tested for three-point bending). The analysis of the defects size, resulting from the dependence (3), shows that for the Si wafers the value of critical defect $c_k \approx 6$ μm (K_{Ic} = 1.3 $MPam^{1/2}$ from Tab. 4, σ_c = 288.9 MPa from Tab. 1, Y = 1.8), while for Y_2O_3 ceramics $c_k \approx 30$ μm (K_{Ic} = 1.8 $MPam^{1/2}$ from Tab. 5, σ_c = 184.3 MPa from Tab. 2).

As mentioned in the Introduction, the defects in the material may be of various form e.g. grain boundaries, microcracks, pores or inclusions of foreign phases. Defects of this kind are commonly present in the ceramic materials, but they do not exist in a pure Si single crystal. According to the literature reports [20], the so-called oxygen precipitates (the regions where inclusions of SiO_x compounds are present) occur in Si. They may have a size from several nm to dozens of nm, while their concentration in the bulk may reach ~ 1×10^9 cm^{-3} [21]. Of course, the dimensions of these defects are much smaller than those calculated above, i.e. 6 μm, but when ones takes into account the value of σ_c = 1.1 GPa from [18], then $c_k \approx 0.4$ μm, which is much closer to the observed precipitate size. Fig. 4 presents a scanning electron microscopic image of the chemically etched surface of the FZ Si sample, where the etched holes are visible as white spots, indicating the possible presence of oxygen precipitates.

The mechanical properties of Si are anisotropic [22] and the cracking energy depends on a given crystallographic plane. Therefore, the fracture toughness K_{Ic} also depends on the crystallographic orientation of the tested sample [22 - 23]. The results of the tests presented in [23] indicate that for the plane (001) K_{Ic} ranges from 0.75 to 1.29 $MPam^{1/2}$. This scatter of the results is mainly due to the use of different research methods. As evidenced by the data presented in Tab. 4, the K_{Ic} value measured by the Vickers method is 0.75 $MPam^{1/2}$, while the K_{Ic} value obtained by the notched beam method is 1.3 $MPam^{1/2}$. The values of the Young's modulus E ranges from 130 to 190 GPa, depending on the crystallographic direction [22 - 23], while the hardness H ranges from 11 - 16 GPa [22]. In Tab. 4, the values of E and H are 173 and 9.9 GPa, respectively. The mechanical properties of the Si single crystal compare favorably with those of Y_2O_3 ceramics. The values of the mechanical parameters other than the fracture toughness are higher for this crystal than those for Y_2O_3 ceramics. However, it should be noted here that other ceramic materials possess better mechanical properties than Y_2O_3 ceramics. For instance, Al_2O_3 ceramics is characterized by the following parameters [24]: $\sigma_c = 413 \pm 43$ MPa, $K_{Ic} = 5.0 \pm 0.4$ $MPam^{1/2}$, E = 380 GPa, and $H = 15 \pm 2$ GPa [8]. On the other hand, for the composite 20% Al_2O_3 - 80% ZrO_2 [25]: $\sigma_c = 1500 \pm 260$ MPa, $K_{Ic} = 5.5 \pm 0.3$ $MPam^{1/2}$, E = 235 ± 12 GPa, H = 15,0 GPa.

The values of subcritical crack growth parameter n, shown in Tab. 6 for Y_2O_3 ceramics, are close to the values obtained by the same method for other ceramic materials, e.g. for Al_2O_3 and Al_2O_3 - ZrO_2 ceramics [24]. However, the value of n = 75.2 for Si is significantly higher than the value of n parameter for the ceramic materials. This fact indicates that the propagation of cracks proceeds here in a narrow range of K_I values, close to the values of K_{Ic}. It can be concluded that, compared to the ceramics, monocrystalline Si is a material more resistant to subcritical cracks growth.

4.2. Comparison of mechanical properties of Si wafers and Y_2O_3 ceramics at elevated temperatures

The obtained results indicate that at 700°C the bending strength of the Si wafers increases more than twice (an increase by 105%). In other words, the material becomes more plastic, as shown in Fig. 5. which means that the destruction of the sample is preceded by the plastic deformation. As shown by the results of the tests presented in [7], at 700°C monocrystalline Si can undergo a deformation due to the generation of dislocations.

The tests of our work proved [7] that the temperature of a Si single crystal transition from a brittle to plastic state at a deformation rate of 2.6×10^{-5} s^{-1} equals ~ 660°C. The tests were carried out at 700°C with a deformation rate of $\sim 5.6 \pm 10^{-5}$ s^{-1}. It should be added that the temperature of this transition increases as a function of deformation rate and depends on the content of the dopants and impurities present in Si single crystals. It was observed that during the cracking the silicon samples disintegrated into a dozen of even dozens of small pieces (while usually into no more than two pieces at room temperature). On the other hand, the K_{Ic} values (measured on a notched bar) are approximately 15 times greater at 700°C than at 20°C. This fact confirms the thesis on the change in the nature of cracking from brittle to plastic. Due to this change, the value of the Weibull modulus increased from m = 4.9 (Tab. 1) at room temperature to 8.9 (Tab. 3) at 700°C which resulted in a significant reduction in the scatter of the obtained experimental results.

Based on the available literature data [26], the mechanism of cracking of silicon samples at 700°C can be proposed as follow. In these samples, the mobile dislocations are generated at 700°C and when the external force becomes increased the length of their displacement path increases too. However, the clusters of oxygen atoms or SiO_x phase precipitations that are present in the material block the dislocation movement. As a result of the dislocation motion blocking, a large stress may arise in many areas of the Si wafer leading to the cleavage of covalent bonds between the neighboring Si atoms. The continuity of the crystal structure of the material gets broken, which is manifested by the disintegration of the wafer into many small pieces.

In the case of Y_2O_3 ceramics, the plastic deformation of the material does not occur and cracking at 800°C is still brittle. The values of K_{Ic} parameter does not change, while bending strength of the material increases by ~ 25% in comparison with the strength measured at room temperature. This increase can be explained by a change in the mechanism of the material cracking. At room temperature, cracking takes place mainly inside the grains. At 800°C, the dominant mechanism of the material destruction is cracking at grain boundaries [10].

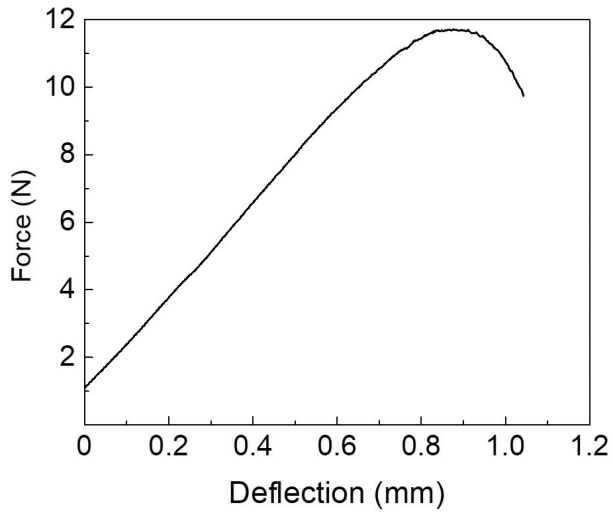

Fig. 5. Relationship between deflection and load, determined during the bending test of a the monocrystalline Si beam at 700°C.
Rys. 5. Krzywa ugięcie-obciążenie, wyznaczona w próbie zginania belki monokrystalicznego Si w temperaturze 700°C.

The analysis of the mechanical properties of a the Si single crystal and Y_2O_3 ceramics at elevated temperatures leads to the conclusion that monocrystalline Si seems to be a better constructional material as compared not only with Y_2O_3 ceramics, but also with other ceramic materials. First of all, it is characterized by a much greater fracture toughness than ceramic materials. The value of K_{Ic} parameter determined in this paper equals ~ 20 $MPam^{1/2}$. It is also noteworthy that the high value of bending strength for the Si single crystal reaches 600 MPa, which is significantly higher than that for Al_2O_3, i.e. ~ 413 MPa [24].

5. Summary

This paper presents the results of investigations of the mechanical properties of Si wafers made from the high-purity Si single crystal obtained by the floating zone (FZ) method. The values of bending strength, fracture toughness, the Young's modulus and material hardness have been determined. The samples were prepared from an n-type silicon single crystal with a crystal orientation <100> and resistivity ~ 2000 Ωcm. The concentration of phosphorus in the Si single crystal was $\sim 3 \times 10^{12}$ cm^{-3} and the concentration of interstitial oxygen atoms was equal to $\sim 5 \times 10^{15}$ cm^{-3}. The bending strength and fracture toughness were determined at both 20°C and 700°C. The mechanical properties of the Si wafers were compared with the properties previously determined for Y_2O_3 ceramics at 20°C and 800°C. Both materials can be used for the production of windows transmitting infrared radiation with the wavelength ranging from 2 μm to 8 μm and the choice of the material for the specific applications may depend on its mechanical properties. It has been found that at room temperature, the fracture toughness of monocrystalline Si is smaller than that of Y_2O_3 ceramics. At the same time, bending strength of the Si single crystal is greater than that of the ceramic material. Based on the literature reports, we have presented a mechanism indicating that the clusters of oxygen atoms or SiO_x precipitates are those defects in the structure of Si, from which the critical crack can start to propagate. At 700°C, monocrystalline Si undergoes the plastic deformation and the dislocations are generated in the material, accompanied by an abrupt increase in the values of the fracture toughness and strength. Fracture toughness and bending strength of the monocrystalline

silicon at temperatures above the temperature of transition from brittle-to-plastic state are probably dependent on the dislocation mobility, and the movement within the crystal may be blocked by the clusters of oxygen atoms or SiO_x inclusions.

Acknowledgements

The results of the research presented in this paper were carried out within the framework of a project financially supported by the research fund of the Institute of Electronic Materials Technology (ITME) in 2017. The project was supervised by Dr. Marek Boniecki. The authors would like to offer special thanks to M.Sc. Magdalena Romaniec for her assistance in taking the samples surfaces images using a scanning electron microscope and to M.Sc. Anna Czerwińska for etching the samples.

References

[1] Ranachowski J.: Elektroceramika: Własności i nowoczesne metody badań, Warszawa – Poznań, PWN, 1981

[2] Guy A. G.: Wprowadzenie do nauki o materiałach, Warszawa, PWN, 1977

[3] Thomson R. M.: Physics of fracture, *J.Phys.Chem. Sol.,* 1987, 48 (11), 965 – 983

[4] Freiman S. W.: Brittle fracture behaviour of ceramics, *Ceram. Bull.,* 1988 , 67(2), 392 – 402

[5] Rećko W. M.: O module Weibulla – historia i przyszłość, *Ceramika/Ceramics*, 2003, 80, 253 – 258

[6] Rećko W. M.: Rozkład Weibulla dla wytrzymałości na ściskanie, *Szkło i Ceramika,* 2008, 59, 2 – 5

[7] Samuels J., Roberts S. G.: The brittle-ductile transition in silicon. I. Experiments, *Proc. R. Soc. London, Ser. A,* 1989, 421, 1 – 23

[8] Munro R. G.: Evaluated material properties for a sintered α-alumina, *J. Am. Ceram. Soc.*, 1997, 80(8), 1919 – 1928

[9] Desmaison-Brut M., Montintin J., Valin E., Boncoeur M.: Influence of processing conditions on the microstructure and mechanical properties of sintered yttrium oxides, *J. Am. Ceram. Soc.*, 1995, 78(3), 716 – 722

[10] Boniecki M., Librant Z., Wesołowski W. et al.: Fracture mechanics of Y_2O_3 ceramics at high temperatures, *Advances in Science and Technology*, 2014, 89, 88 – 93

[11] Nigara Y.: Measurement of optical constants of yttrium oxide, *Jpn. J. Appl. Phys.,* 1968, 7, 404 – 408

[12] Harris Daniel C.: Materials for infrared windows and domes: properties and performance, SPIE – The International Society for Optical Engineering, Bellingham, Washington 1999, 150 – 191

[13] Boniecki M., Jach K., Librant Z., et al.: Mechanika kruchego pękania ceramiki Y_2O_3, *Materiały Ceramiczne/Ceramic Materials*, 2015, 67, 1, 43 – 47

[14] Boniecki M., Librant Z., Wesołowski W. et al.: Odporność na pękanie ceramiki Y_2O_3, *Materiały Ceramiczne/Ceramic Materials*, 2015, 67, 4, 378 – 382

[15] Fett T., Munz, D.: Subcritical crack growth of macrocracks in alumina with R-curve behavior, *J. Am. Ceram. Soc.*, 1992, 75, 4, 958 – 963

[16] Anstis G. R., Chantikul P., Lawn B. R., Marshall D. B.: A critical evaluation of indentation techniques for measuring fracture toughness: I. Direct crack measurements, *J. Am. Ceram. Soc*., 1981, 64, 9, 533 – 538

[17] Wiederhorn S. M.: Subcritical crack growth in ceramics, Fracture Mechanics of Ceramics v.2, ed. by Bradt R.C., Hasselman D. P. H., Lange F. F., New York, London, Plenum Press, 1974, 613 – 646

[18] Vedde J., Gravesen P.: The fracture strength of nitrogen doped silicon wafers, *Mater. Sci. Eng.*, 1996, B36, 246 – 250

[19] Dziubak C., Rećko W. M.: Statystyka wytrzymałości ceramiki korundowej, *Szkło i Ceramika*, 2009, 60, 7 – 11

[20] Zeng Y., Ma X., Chen J., Yang D.: Correlation between oxygen precipitation and extended defects in Czochralski silicon: Investigation by means of scanning infrared microscopy, *J. Electronic. Mater*. 2010, 39 (8), 648 – 651

[21] Achmetov V. D., Richter H., Lysytskiy O., Wahlich R., Muller T.: Oxide precipitates in annealed nitrogen-doped 300 mm CZ-Si, *Mater.Sci. Semiconductor Processing*, 2003, 5, 391 – 396

[22] Ebrahimi F., Kalwani L.: Fracture anisotropy in silicon single crystal, *Mater. Sci. Eng.* 1999, A268, 116 – 126.

[23] Masolin A., Bouchard P. O., Martini R., Bernacki M.: Thermo-mechanical and fracture properties in single-crystal silicon, *J. Mater. Sci*. 2013, 48, 979 – 988

[24] Boniecki M.: Wpływ mikrostruktury na rozwój mikropęknięć podkrytycznych w materiałach ceramicznych, *Materiały Elektroniczne – Electronic Materials*, 1992, 1 (77), 8 – 29

[25] Boniecki M., Gołębiewski P., Wesołowski W., et al.: Kompozyt Al_2O_3 – ZrO_2 wzmocniony płatkami grafenowymi, *Materialy Elektroniczne – Electronic Materials*, 2016, 44, 1, 20 – 28

[26] Hu S. M.: Dislocation pinning effect of oxygen atoms in silicon, *Apl. Phys. Lett.* 1977, 31 (2), 53 – 55

Investigation of oxide crystals by means of synchrotron and conventional X-ray diffraction topography

Wojciech Wierzchowski[1], Agnieszka Malinowska[1], Krzysztof Wieteska[2], Edyta Wierzbicka[1], Krystyna Mazur[1], Maria Lefeld - Sosnowska[3], Marek Świrkowicz[1], Tadeusz Łukasiewicz[1]

X-ray diffraction topography, exploring both conventional and synchrotron sources of X-rays, has been widely used for the investigation of the structural defects in crystals of oxides. The majority of bulk oxide crystals have been grown by the Czochralski method from a melted mixture of high purity oxides. Some important oxide crystals like quartz and ZnO have been obtained by the hydrothermal method. In the case of crystals grown by the first method, synchrotron diffraction topography can be and was used for studying individual dislocations and their complexes (e.g. glide bands, sub-grain boundaries), individual blocks, twinning, the domain structure and various segregation effects negatively affecting crystal properties. What is more, the topographical investigation can provide information concerning the reasons for the generation of the defects, which becomes useful for improving the growth technology. In the present paper the possibilities of the diffraction topography are discussed on the basis of several investigations of the oxide crystals, in particular garnets, orthovanadates, mixed calcium barium and strontium niobates as well as praseodymium lanthanum aluminates. The majority of the results refer to oxide crystals grown at the Institute of Electronic Materials Technology (ITME). The synchrotron investigations included in the paper were performed by the authors at the HASYLAB Synchrotron Laboratory in Hamburg.

Key words: X-ray diffraction topography, crystal lattice defects, Czochralski method

Badanie monokryształów tlenkowych za pomocą synchrotronowej i konwencjonalnej rentgenowskiej topografii dyfrakcyjnej

Rentgenowska topografia dyfrakcyjna, wykorzystująca zarówno konwencjonalne, jak i synchrotronowe źródła promieniowania rentgenowskiego, jest od wielu lat z powodzeniem stosowana do badania defektów strukturalnych w różnego rodzaju monokryształach. Szeroką grupę tych materiałów stanowią kryształy tlenkowe, które w większości są otrzymywane metodą Czochralskiego ze stopionej mieszaniny tlenków o wysokiej czystości. Do otrzymywania kryształów tlenków, takich jak kwarc i ZnO, stosuje się metodę hydrotermalną. Rentgenowska topografia dyfrakcyjna może być wykorzystana do badania indywidualnych dyslokacji i ich kompleksów (np. pasma poślizgowe, granice niskokątowe), pojedynczych bloków, zbliźniaczeń, struktury domenowej i różnych efektów segregacyjnych. Wszystkie te defekty mogą wpływać negatywnie na jednorodność i właściwości kryształów. Badania topograficzne mogą również dostarczyć informacji dotyczących przyczyn powstawania defektów, co przydatne jest w doskonaleniu technologii. W niniejszej pracy omówiono możliwości topografii dyfrakcyjnej na podstawie przeprowadzonych badań szeregu kryształów tlenkowych, w szczególności granatów, ortowanadianów, mieszanych niobianów wapnia, baru i strontu oraz glinianów prazeodymu i lantanu. Większość wyników dotyczy monokryształów tlenków otrzymywanych w Instytucie Technologii Materiałów Elektronicznych (ITME). Uwzględnione badania synchrotronowe zostały przeprowadzone przez autorów w Laboratoriom Synchrotronowym HASYLAB w Hamburgu.

Słowa kluczowe: dyfrakcyjna topografia rentgenowska, defekty sieci krystalicznej, metoda Czochralskiego

1. Introduction

The important group of crystals, which is widely used for several applications, particularly in the laser technology and in the technology of electronic devices are oxide crystals, built either from single oxides or a mixture of oxides [1 - 11]. These crystals provide an important field for the application of X-ray diffraction topography exploring both conventional and synchrotron radiation sources.

The majority of oxide crystals are not soluble in water in normal conditions and they are useful for the preparation of durable elements, convenient for most of the applications. The majority of the bulk oxide crystals are therefore grown by the Czochralski method from a melted mixture of high purity oxides. Only some of them are obtained by means of the floating zone method (recently also with optical heating) [5 - 6]. Some important oxide crystals like quartz and ZnO [7 - 11] are grown by the hydrothermal method. In the last case the crystal grow

[1] Institute of Electronic Materials Technology, Wólczyńska 133, 01-919 Warsaw, Poland, e-mail: wojciech.wierzchowski@itme.edu.pl
[2] National Centre for Nuclear Research, Sołtana 7, 05-400 Otwock-Świerk, Poland
[3] Institute of Experimental Physics, University of Warsaw, Pasteura 5, 02-093 Warsaw, Poland

from an aqueous solution, formed under high pressure at high temperatures. The crystals obtained by means of the hydrothermal method are to some extend analogous to those obtained from an aqueous solution, containing various growth sectors corresponding to some low indexed crystallographic planes. The differences in growth rates and segregation parameters for the various growth planes result in differences of lattice parameters and segregation effects, usually causing the strains in the growth sector boundaries. The Bridgman, flux and Verneuils methods have also been sometimes used [12].

X-ray diffraction topography [12 - 24] is a method, which can be effectively used for the characterization of oxide crystals. It includes in fact a number of methods differing in the experimental arrangement and consequently in the mechanism of contrast formation and in the sensitivity. The general principle of the methods consists in recording contrast inhomogeneities in the diffracted beam due to long range strain fields related to lattice defects/crystal deformations with a very high spatial resolution. The forward diffracted one could also be used, but it happens rather rarely.

X-ray diffraction topographic methods enable the identification of the defects, especially dislocations, stacking faults and regularly shaped inclusions. The identification of the defects in X-ray diffraction topography includes the analysis of contrast extinction in various crystallographically equivalent reflections and simulation of the topographic contrasts [12 - 14]. The topographic methods are usually more effective with the synchrotron radiation than with the conventional radiation thanks to the possibility of better resolution, a better collimation and an access to more suitable wavelength forming the image [25 - 30]. The numerical simulation of diffraction contrast [12 - 14] can presently be used practically in the case of all topographic methods.

A significant new step in the development of the laboratory based diffraction topography was the recent introduction of a new Micron XRT apparatus from Rigaku [26 - 27]. The equipment uses a fine focus rotating generator and a special parabolic mirror forms a nearly parallel beam. High intensity of the beam enables the use of a CCD camera with resolution close to 2 μm.

Conventional topographic investigations of the Czochralski-grown oxide crystals have been published in [33 - 41], while the crystal grown by the hydrothermal method in [45 - 54]. Synchrotron topographic investigations of oxide crystals have been published in [36 - 46, 63], in particular by Baruchel et al. [45], Kasper et al. [46], Yao et al. [47], Muehlberg et al. [48], Prokhorov et al. [49], Yoneda et al. [50] and by Dudley and Yao [51 - 52] and Malinowska et al. [55]. An interesting synchrotron topographic method is so called *stroboscopic topography* [53 - 54]. It can be carried out in the piezoelectric crystals, particularly lithium niobates and it reveals the strain which appears in the course of the induced oscillations.

The present paper will illustrate the possibilities of the conventional and synchrotron X-ray topography for the Czochralski-grown crystals as well as some more detailed experimental problems being the result of the investigations performed by the authors, and published elsewhere [55 - 72]. These results include synchrotron topographic investigations performed at HASYLAB, the details of which are described in [57].

2. Growth of oxide crystals

The most popular method of growing the oxide crystal is the Czochralski method, in which the crystals are grown from the suitably composed mixture of melted oxides. However, recently the floating-zone method including optical heating furnaces instead of the inductive coils [5 - 6] has also been applied. The equipment used for the growth of single crystals from melted oxides by the Czochralski method is shown in Fig. 1a, while the schema of the floating-zone

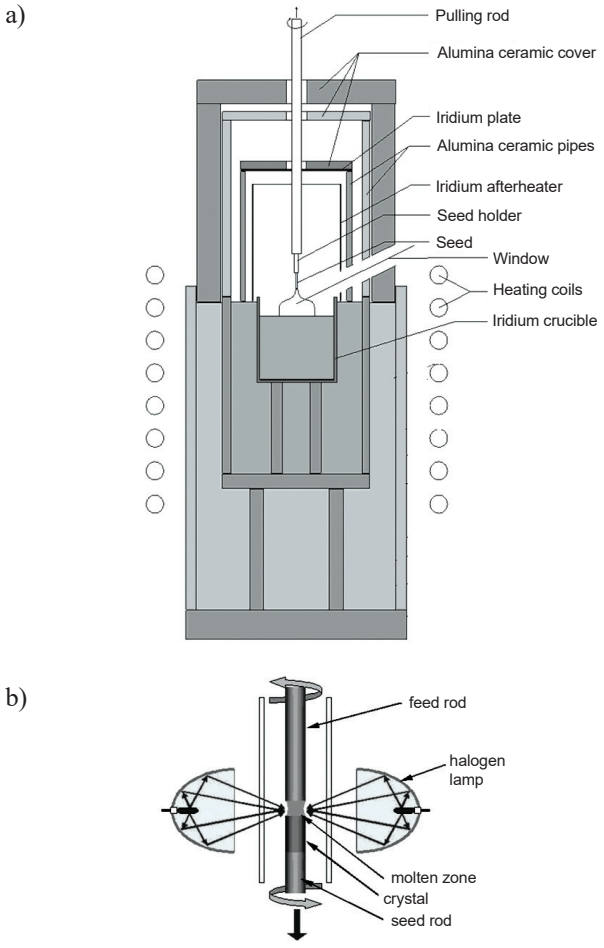

Fig. 1. Most frequently used methods of oxide crystals growth: (a) the Czochralski method, (b) the optical floating zone method [5, 81].
Rys. 1. Najczęściej stosowane metody wzrostu kryształów tlenkowych: (a) metoda Czochralskiego, (b) metoda topienia strefowego [5, 81].

method with optical heating is shown in Fig. 1b. In the hydrothermal method the crystals are grown from aqueous solutions obtained at high temperatures and under very high pressure. The last method was used in specific cases, e.g. for growing quartz and zinc oxide crystals.

Experimental results included in the present paper have been obtained with crystals grown by the Czochralski method and by the hydrothermal method in the Institute of Electronic Materials Technology. In the first case the oxide crystals were grown in an inductively heated iridium or platinum crucible and with a passive after heater. Starting materials with 4N purity were heated at the temperatures up to 1000°C for 6 hours before weighing, mixing and melting. The initial composition should compensate the effects of eventual evaporation. Single crystals with 20 mm diameter were grown on iridium 2 mm rod with the pulling rate of 3 - 4 mm/h and the rotation of 4 - 6 rpm. Crystals were grown under ambient pressure in a nitrogen atmosphere, but sometimes the growing atmosphere contained an admixture of oxygen.

3. X-ray diffraction topography

The X-ray conventional topography of oxide crystals is usually carried out by means of two most popular methods. The most effective single crystal method (shown schematically in Fig. 2a) has been proposed by Lang [15 - 16], while the double-crystal topographic method (Fig. 2b) has been proposed by Bond and Andrus [17] but

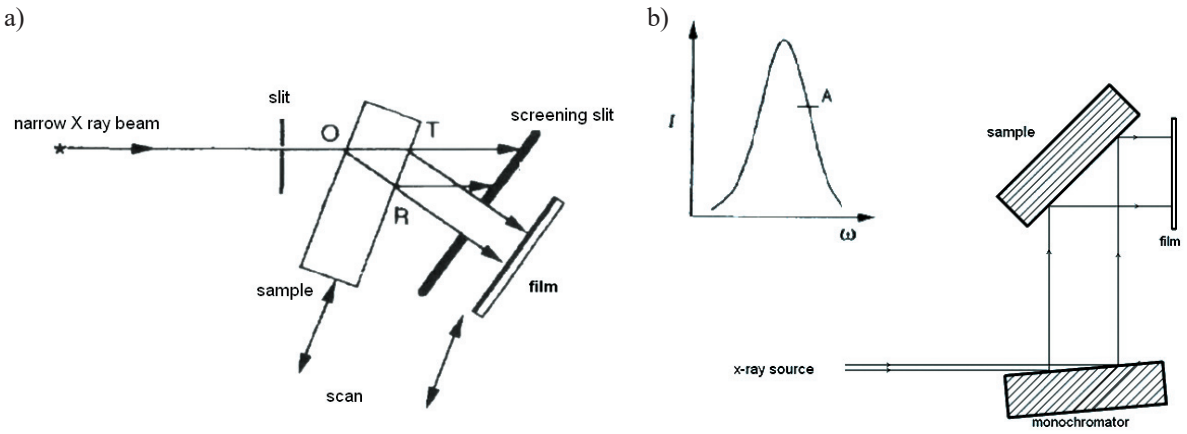

Fig. 2. Schema of the two most important topographic methods of the conventional X-ray diffraction topography: (a) the Lang projection (and section) topography [15 - 16], and (b) the double crystal topography – the schema of the arrangement, with significantly asymmetric reflection at the monochromator proposed by Renninger [20].
Rys. 2. Schematy dwóch najważniejszych metod konwencjonalnej rentgenowskiej topografii dyfrakcyjnej: (a) projekcyjna (i przekrojowa) topografia Langa [15 - 16], i (b) topografia dwukrystaliczna – schemat układu z asymetrycznym odbiciem na monochromatorze zaproponowany przez Renningera [20].

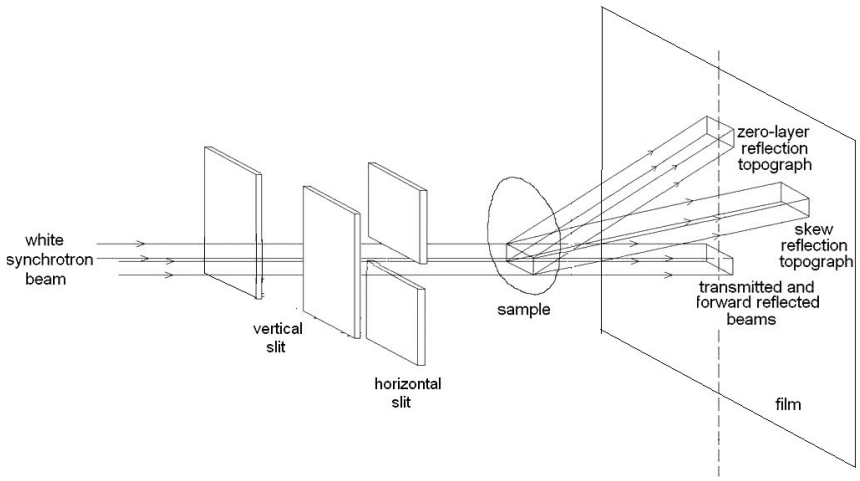

Fig. 3. The scheme of the synchrotron white beam topography in transmission case [57].
Rys. 3. Schemat synchrotronowej topografii w wiązce białej dla przypadku transmisyjnego [57].

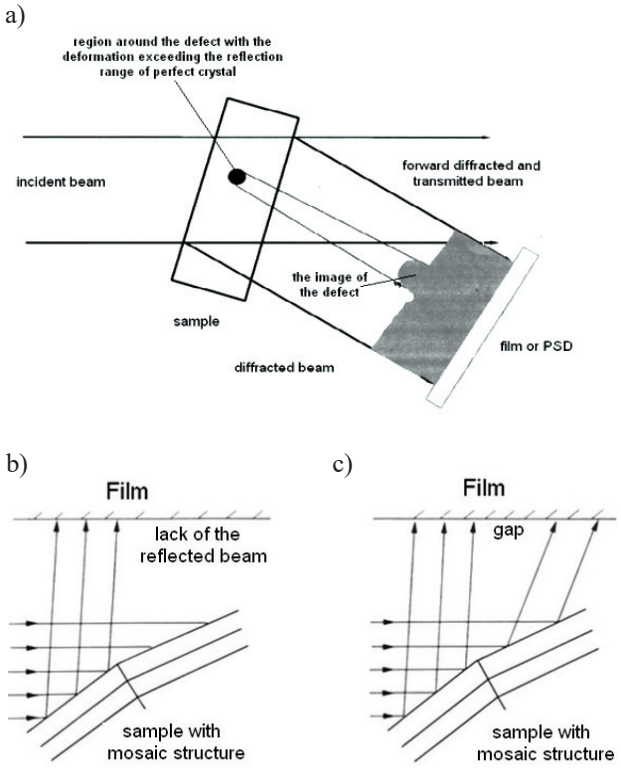

Fig. 4. Schema of contrast formation in the X-ray diffraction topography: (a) – reproduction of isolated defects surrounded by almost perfect crystal (transmission case), (b), (c) formation of contrast from differently oriented parts of the crystals, respectively in the monochromatic and white beam of X-rays. According to [12 - 14, 78].

Rys. 4. Schemat powstawania kontrastu w rentgenowskiej topografii dyfrakcyjnej: (a) – przypadek transmisyjny dla pojedynczego defektu w krysztale prawie idealnym, (b), (c) tworzenie kontrastu dla różnie zorientowanych części kryształu, odpowiednio dla wiązki monochromatycznej (b) i białej (c) promieniowania X. Na podstawie [12 - 14, 78].

effectively used for revealing the dislocations by Bonse and Keppler [18]. The further extensions of the double--crystal method were described in [19 - 21]. The earlier topographic methods were revealed by Shultz [17], Berg [18] and Barrett [19].

Bending magnets were the sources of the synchrotron radiation in the case of presently described topographic experiments at DORIS III. They allowed obtaining the photon energy in the range from 5 to 35 keV. The energy was satisfactory for most of the topographic investigation. The present investigations of the oxide crystals were carried out at the two experimental stations at HASYLAB, the white beam station F1 and the monochromatic beam station E2 [57].

A schema of the arrangement for synchrotron white beam topography is shown in Fig. 3. The beam limited by a system of vertical and horizontal slits is entering the crystals providing a kind of Laue pattern either in the Laue-case (transmission) or Bragg-case (reflection). Thanks to small apparent diameters of the synchrotron source, of approximately 0.5 mm in vertical direction and 2 mm wide and large 18 m distance of the experimental station from the bending magnet, each Laue spot is a high resolution topograph revealing the defects in the investigated crystal. At the typical distances of film to crystal of 15 cm the geometrical resolution is better than 5 μm. The synchrotron topographic investigations were usually performed both in the back-reflection and in the transmission case, exposing the projection and section topographs. In the case of the section topography it was possible to reduce the width of the slit to 5 μm.

Most often the so called *extinction contrast* is formed in a single crystal white beam projection topography in the Bragg - case and in the Laue - case at small absorption. The defects are revealed thanks to the additional intensity contributed by a region of defect *outside the reflection range* fulfilling the condition [24, 54]:

$$|4\sin\Theta \frac{\partial \vec{u}(\vec{r}) \cdot \vec{h}}{\partial s_h}| > \delta. \qquad (1)$$

Here $\vec{u}(\vec{r})$ is the displacement vector connected with the defect, $\vec{h}$ is the diffraction vector and s_h is the coordinate along the reflected beam. This condition indicates that wider images of dislocations can be obtained when the width of the reflection range is small. The very important parameter, characterizing the possibilities of revealing the defects is the range of reflection predicted by the dynamical theory [9]:

$$\delta = \frac{2|C|}{\sin(2\vartheta_b)} \sqrt{\frac{\gamma_0}{|\gamma_h|} \chi_h \chi_{\bar{h}}}. \qquad (2)$$

The polarization factor $C = |\cos 2\Theta|$ for the π-polarization in the plane of diffraction and $C = 1$ for σ-polarization perpendicular to the plane of diffraction, $\chi_{h,0}$ are the coefficient of the Fourier expansion of dielectric susceptibility, proportional to the structural factors.

The anomalous transmission contrast (also called dynamical contrast) is observed when attenuation is strong – and the defects become revealed thanks to the destruction of the *anomalous transmission*. The last effect consists in fitting the excited wave-field to the reflecting planes causing a significant decrease of absorption. Due to the anomalous transmission it is otherwise possible to obtain the transmission topographs in highly absorbing crystals built of the element with large atomic number, as the anomalous absorption can be even of two orders lower than the normal photoelectrical absorption. In addition the synchrotron sources offer another great help in studying such crystals, as they give the possibility to use reflections fulfilling the Bragg condition for very short wavelength and thus with low absorption.

A different contrast mechanism is present in the case of the double-crystal topography, which may be interpreted as the result of local shifts of the rocking curve

angular position (with respect to a reference area) caused by the strain field (for example dislocations) or chemical compositions changes (segregation effects). The observed change of the reflected intensity ΔI may be written [17]:

$$\Delta I = \frac{dP(\Theta)}{d\Theta}\left[\frac{\Delta d}{d}\,\mathrm{tg}\Theta + \Delta\Theta_g\right]. \qquad (3)$$

The first term describes the change of the Bragg angle and the second the misorientation component in the plane of diffraction. The derivative of rocking curve $P(\Theta)$ is taken at the angular setting where the topograph is exposed. This means that the contrast strongly depends on the angular setting. It is the strongest on the steep slopes of the rocking curve and inverts coming to the opposite slope. In some cases the topographs taken at the slope allow to reveal the relative lattice parameter changes $\Delta a/a$ on the level 10^{-8}.

An oxide crystal can have different chemical composition, which influence the width of reflection and the contrast of the defect images. In general the X-ray diffraction topography provides weaker contrast on dislocations and other defects in the case of the crystals built of the atoms with larger atomic number.

The images of individual defects are often accompanied by some interference effects often caused by the decomposition of wave-fields. Obtaining the theoretical simulated images reproducing such fringes is possible with the use of numerical integration of the Takagi-Taupin equations [14].

The white beam synchrotron topography is more strictly equivalent to the Shultz [22] method than to the conventional Lang method, especially in the case when the crystal contains several disoriented parts. The white-beam topographic images of almost perfect crystals containing individual defects are, however, very similar to those obtained using the Lang method. The most important element of the setup used for synchrotron monochromatic beam topography was the monochromator equipped with two silicon crystals using respectively 333 and 511 reflections, but in many aspects the method is similar to the conventional double crystal topography.

In the case of highly deformed, e.g. elastically bent samples, the double-crystal topography and synchrotron monochromatic beam topography are often highly restricted to a narrow stripe. In such situations the so called *zebra pattern* technique [21] is very helpful, where a series of exposures with step-wise altered angular position is recorded on the same film.

4. Discussion of the representative results

The first representative examples of the use of X-ray diffraction topography refer to the crystals newly developed at ITME. Figs. 5 and 6 present the representative X-ray diffraction topographs of the $MgAl_2O_4$ samples obtained using the Lang and double crystal method including the zebra pattern technique [79]. The crystal in Fig. 5 contained the core formed of several facets and a number of volume defects – most of them are solute trails around the core and close to the crystal boundaries. The representative X-ray diffraction topographs

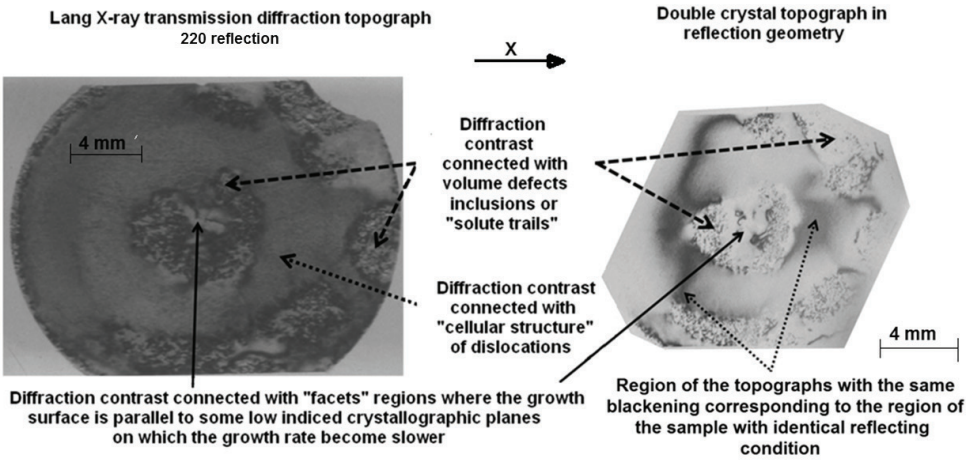

Fig. 5. The representative X-ray diffraction topographs obtained respectively using the Lang transmission method (220 reflection, Mo$K\alpha_1$) and the double crystal method (533 reflection, Cu$K\alpha_1$) the sample cut out from the $MgAl_2O_4$ crystal with 0.135 at. % of cobalt. The crystal contains the rod formed of several facets and a number of volume defects around the rod and close to the crystal boundaries – most of them are the solute trails. According to [79].

Rys. 5. Wybrane rentgenowskie topogramy dyfrakcyjne próbki $MgAl_2O_4$ 0,135 % at. Co wykonane metodą transmisyjnej topografii Langa (refleks 220, Mo$K\alpha_1$) oraz metodą topografii dwukrystalicznej (refleks 533, Cu$K\alpha_1$). Kryształ zawiera rdzeń utworzony przez obszary ściankowane oraz dużą ilość defektów objętościowych wokół rdzenia i blisko brzegu kryształu – wiele z nich to defekty typu *solute trials*. Na podstawie [79].

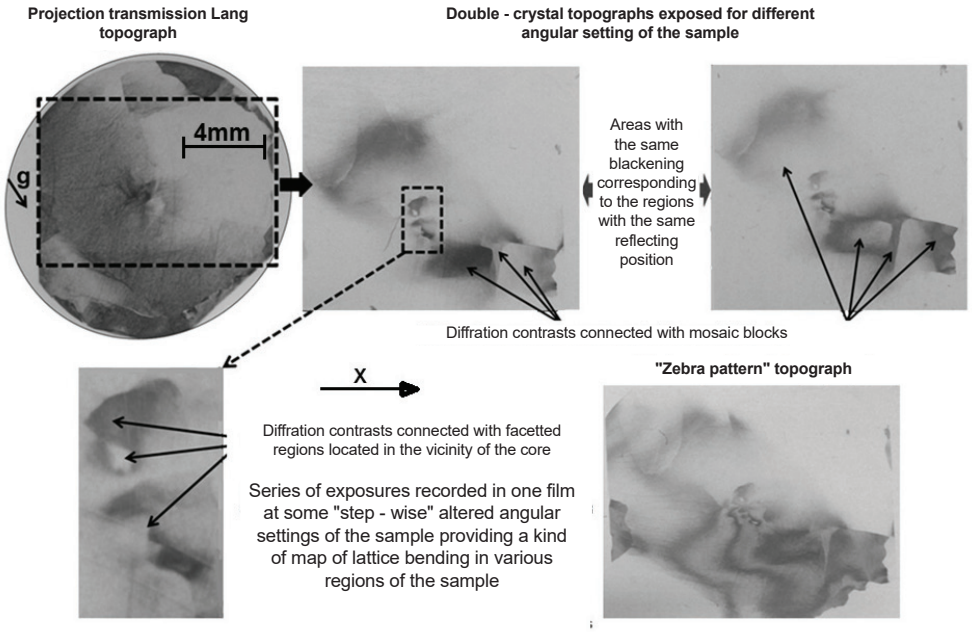

Fig. 6. The representative X-ray diffraction topographs obtained using the Lang transmission method in 220 reflection (MoKα_1 radiation) and the double crystal method (including the zebra pattern technique) in 533 reflection (CuKα_1 radiation) of another sample cut out from the $MgAl_2O_4$ crystal with 0.286 at. % of cobalt. The crystal contains a similar rod as in Fig. 5 and a number of volume defects as solute trails around the rod and close to the crystal boundaries. Additionally some slightly disoriented grains are revealed. According to [79].
Rys. 6. Wybrane rentgenowskie topogramy dyfrakcyjne próbki $MgAl_2O_4$ 0,286 % at. Co wykonane metodą transmisyjnej topografii Langa (refleks 220, promieniowanie MoKα_1) oraz metodą topografii dwukrystalicznej (łącznie z techniką typu *zebra pattern*) (refleks 533, promieniowanie CuKα_1). Kryształ zawiera podobny rdzeń jak w przypadku próbki z Rys. 5. oraz dużą ilość defektów objętościowych typu *solute trials* otaczających obszar rdzenia oraz występujących blisko brzegu kryształu. Na podstawie [79].

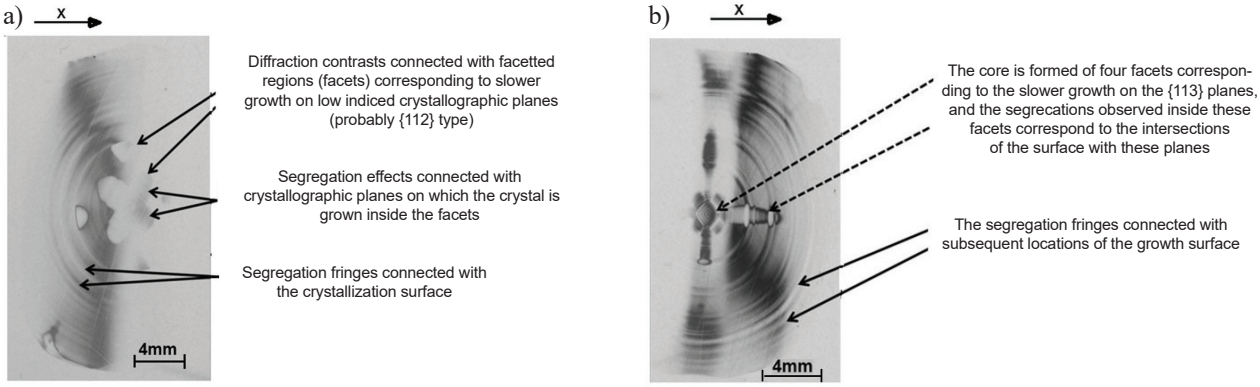

Fig. 7. Conventional double crystal topographs in 840 reflection in CuKα_1 of the samples cut out from two LuYAG crystals, doped with 0.2 at.% (a) and 0.16 at.% (b) of praseodymium, revealing segregation fringes and some sets of facetted regions corresponding to various low indexed crystallographic planes, where the growth rate becomes slower. According to [80].
Rys. 7. Konwencjonalne topogramy dwukrystaliczne (refleks 840, promieniowanie CuKα_1) próbki LuYAG domieszkowanej 0,2% at. Pr (a) i 0,16% at. Pr (b). Topogramy ujawniają prążki segregacyjne oraz pewne układy obszarów ściankowanych odpowiadających wolniejszemu wzrostowi na płaszczyznach krystalograficznych o niskich wskaźnikach. Na podstawie [80].

of another sample are presented in Fig. 6. It was cut out from the $MgAl_2O_4$ crystal containing the similar rod. In this case there was a number of volume defects trails around the rod and close to the crystal boundaries, but additionally some slightly disoriented grains were also visible.

In Fig. 7 we report some representative double crystal topographs of $(Lu_{0.75}Y_{0.25})_3Al_5O_{12}$ (LuYAG-75) crystals [80], which are new materials developed for modern scintillator crystals intended to be used for positron generation tomography, as well as for some spaceship probes. In this case, a very high attenuation of the molybdenum and copper radiation by yttrium, lutetium, and praseodymium admixture significantly disturb the possibility of making the conventional transmission topographs, but the defects may be successfully revealed by the double crystal topographic method.

The presently developed technology enabled obtaining very efficient $(Lu_{0.75}Y_{0.25})_3Al_5O_{12}$ (LuYAG-75) and $Lu_3Al_5O_{12}$ (LuAG) scintillators. As it may be seen in Fig. 7,

the characteristic defects in these crystals are the distinct segregation fringes and various facets – the regions where the crystallization surface become parallel to some low indexed crystallographic planes, on which the growth rate become slower [80]. The last phenomenon is responsible for the characteristic appearance of the crystals grown from solutions, but also from vapour and the melt.

The formation of the facets was effectively followed by the complementary use of the projection synchrotron topography and synchrotron section topography, which allowed fitting the regions of facets and actual inclination of the growth surface in the case of $Yb_3Al_5O_{12}$(YbYAG) crystals [66]. The topographs presenting a typical set of facets for two differently shaped growth surfaces are shown in Fig. 8.

The observed facets formed characteristic patterns, differing in different samples. It is well known that the most probable reason of facet formation is the coincidence of the orientation of growth surfaces with low indexed crystallographic planes. The growth velocity is usually slower in the direction perpendicular to these planes leading to slower growth in facetted regions and the constitutional supercooling. The facets may be identified as corresponding to {221}, {211}, {311} and {301} planes as it is shown schematically in Fig. 9. The first three {221} facets usually form a core, observed in most of the crystals, sometimes neighbouring with {211} ones. The third type of facets corresponds to the planes inclined at 43º and it occurs mostly for convex growth surface. The identification of the facets was confirmed by the transmission section topographs shown in Fig. 10, that allowed the observation of the location of the growth bands in the intersection of the sample with the incident synchrotron beam. It should also be noted that the topograph in Fig. 10b

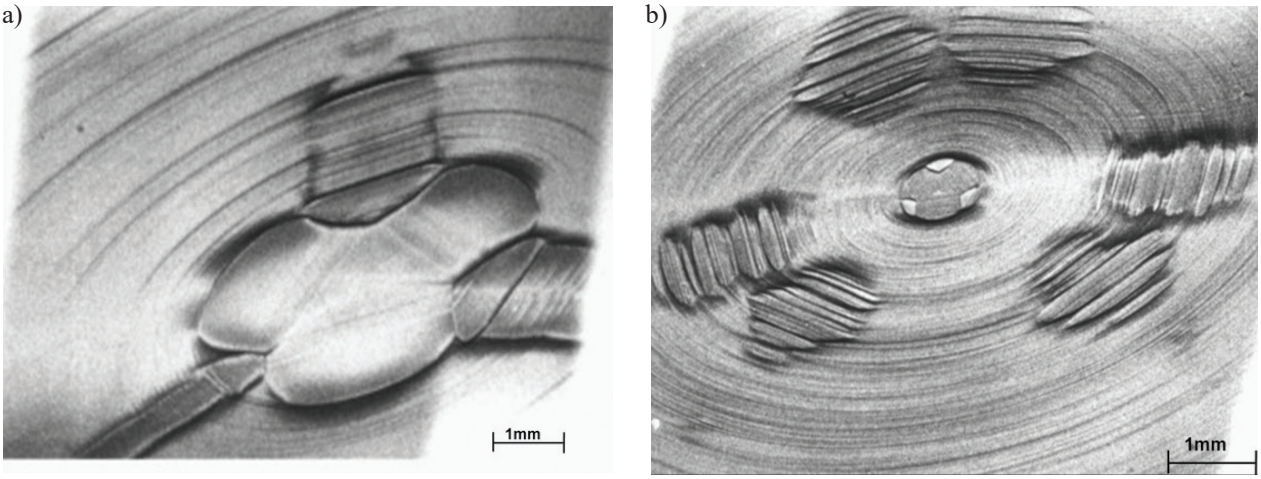

Fig. 8. White beam projection reflection topographs of Er-doped $Yb_3Al_5O_{12}$ crystals revealing segregation fringes and sets of facets; doping level: (a) 10 at. % Er and (b) 1.5 at. % Er; (a) 422 reflection, 0.0872 nm radiation, (b) 112 reflection, 0.4 nm radiation. According to K. Kołodziejak et al. [66].
Rys. 8. Odbiciowe topogramy projekcyjne w wiązce białej monokryształów $Yb_3Al_5O_{12}$ domieszkowanych erbem (10 % at. (a) i 1,5 % at. (b)) ujawniające prążki segregacyjne i układy obszarów ściankowanych; (a) refleks 422, promieniowanie 0,0872 nm, (b) refleks 112, promieniowanie 0,4 nm. Na podstawie K. Kołodziejak i in. [66].

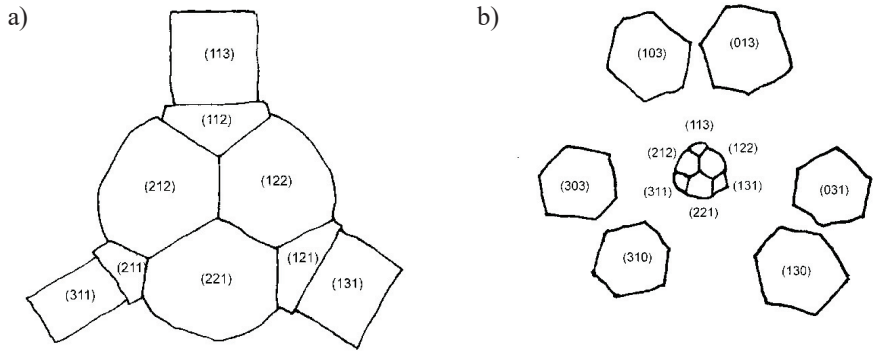

Fig. 9. (a), (b)The schema of identified facets corresponding respectively to the topographs in Fig. 8a, and b. According to K. Kołodziejak et al. [66].
Rys. 9. Schematy układu ścianek z przypisanymi wskaźnikami odpowiadające topogramom z Rys. 8a i 8b. Na podstawie K. Kołodziejak i in. [66].

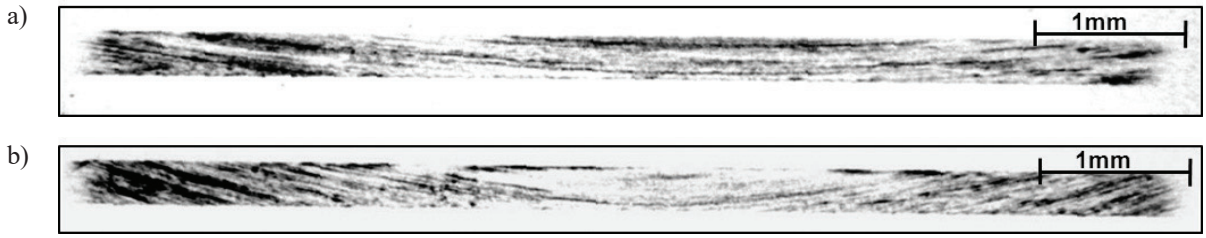

Fig. 10. Transmission white-beam section topographs of Er-doped $Yb_3Al_5O_{12}$ samples taken in $(\bar{1}6\bar{1}1)$ reflection, of 0.052 nm radiation and revealing the striation fringes corresponding to the successive location of growth surfaces in the plane intersected by the narrow incident beam perpendicular to the sample. Doping level: (a) 30 at. % and (b) 1.5 at. %. Thickness of both samples is 550 μm, the horizontal edge of the topographs is 8 mm. According to K. Kołodziejak et al. [66].
Rys. 10. Transmisyjne przekrojowe topogramy w wiązce białej monokryształów $Yb_3Al_5O_{12}$ domieszkowanych erbem (30% at. (a) i 1,5% at. (b)); refleks $(\bar{1}6\bar{1}1)$, promieniowanie 0,052 nm. Topogramy ujawniają prążki segregacyjne odpowiadające kolejnym położeniom powierzchni wzrostu w płaszczyźnie przecięcia kryształu wąską wiązką padającą prostopadle do próbki. Grubość próbek 550 μm, szerokość poziomej krawędzi topogramu – 8 mm. Według K. Kołodziejak i in. [66].

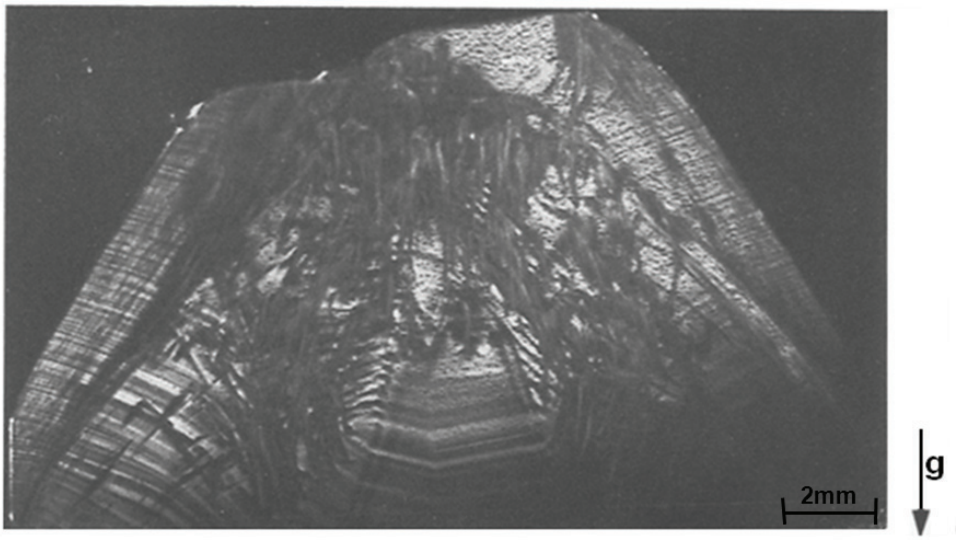

Fig. 11. Representative Lang topograph (direct copy) of the sample cut out along the growth axis from the initial part of the YAG crystal; 440 reflection, CuKα_1 radiation. According to K. Mazur and W. Wierzchowski [56].
Rys. 11. Wybrany topogram Langa (kopia bezpośrednia) próbki wyciętej równolegle do osi wzrostu z części początkowej kryształu YAG; refleks 440, promieniowanie CuKα_1. Według K. Mazur i W. Wierzchowski [56].

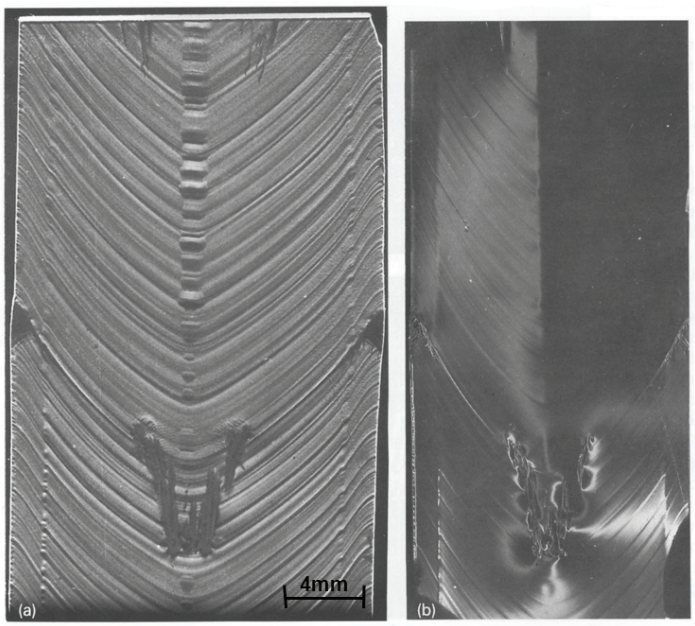

Fig. 12. (a) Lang topograph of the sample cut along the [111] growth axis from the middle part of Nd doped YAG crystal; 422 reflection, CuKα_1 radiation. The diffraction vector is located horizontally; (b) the double crystal topograph of the thicker sample cut close to that shown in (a); exposition in 620_{Si}-888_{YAG} arrangement, direct copies. According to K. Mazur and W. Wierzchowski [56].
Rys. 12. (a) Topogram Langa próbki wyciętej równolegle do osi wzrostu [111] ze środkowej części kryształu YAG:Nd; refleks 422, promieniowanie CuKα_1. Kierunek wektora dyfrakcji w poziomie; (b) topogram dwukrystaliczny grubszej próbki wyciętej w pobliżu próbki (a); ekspozycja w układzie 620_{Si}-888_{YAG}, kopia bezpośrednia. Na podstawie K. Mazur i W. Wierzchowski [56].

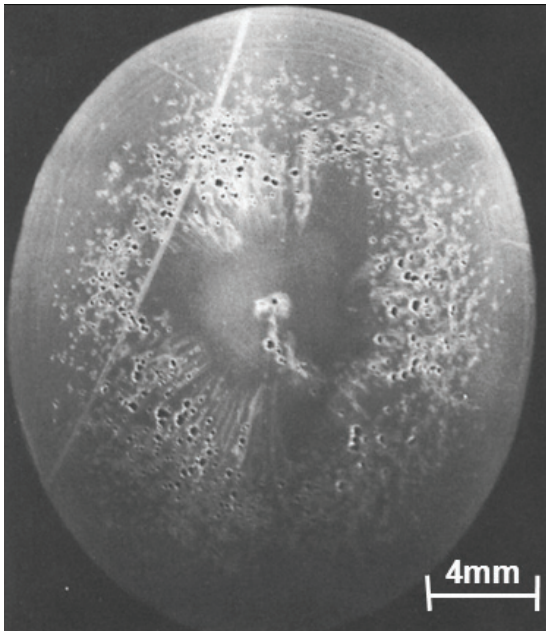

Fig. 13. Berg-Barrett topograph of the YAG sample exhibiting *reflecting* and *not-reflecting* volume defects, corresponding to *solute trails*; 751 reflection, CuKα_1 radiation, direct copy. According to K. Mazur and W. Wierzchowski [56].
Rys. 13. Topogram Berga-Barretta próbki YAG ujawniający *odbijające* i *nieodbijające* defekty objętościowe odpowiadające s*olute trails*; refleks 751, promieniowanie CuKα_1, kopia bezpośrednia. Według K. Mazur i W. Wierzchowski [56].

reveals some black dot-like contrasts, which may correspond to dislocations [66].

The representative transmission topograph of the samples cut out from the initial parts of the $Y_3Al_5O_{12}$ (YAG) crystals is shown in Fig. 11 [56]. We may notice that in the majority of crystals the growth surface is parabolic. At the very first stages of the growth, the surface is relatively flat and the core is not present. It starts to appear when the growth surface becomes more concave. Inside facets the growth bands are inclined at approximately 20° to the (111) plane. That is consistent with the arrangement of facets seen in the topographs of the samples perpendicular to the growth axis and points that the facets correspond to {112} planes. The topographs exhibit sequences of growth bands, corresponding to the growth conditions changes. Following the equivalent parts of growth bands with an analogous pattern from the core inside and in the rest of the crystal it may be found that the core grew a little deeper in the melt, probably in the zone where the stream of convection is pointing down to the melt. In many cases also the change of the growth bands curvature is observed at the distance approximately 1/3 of the crystal radius from the crystal boundaries. This curvature change also corresponds most probably to the zones with different directions of convection at the growth surface.

In the transmission topograph shown in Fig. 11 we may notice that the volume defects have in fact the form of thin long pipes. We can notice that they are grouped into a number of fan-shaped beams, running in different directions. It is difficult to absolutely exclude the existence of dislocations between the pipe-shaped volume defects. It is rather unlikely, however, as no contrasts in the double--crystal topographs resemble the rosettes characteristic for the dislocations outcrops.

In Fig. 12 we report double-crystal and transmission topographs of the neighboring samples, corresponding to same intersection of the crystal parallel to the growth axis. Here the two samples, a thinner one and a thicker, were cut out one close to the other [56]. The thin sample was used for the Lang transmission topography, while the other 1.5 mm thick for the double-crystal topography. The double-crystal topograph shows significant strains connected with the core. After cutting out the samples these strains expanded causing the misorientation of the two parts of the sample located on both sides of the core, which made one half of the sample stay out of reflection. We may notice in the topographs shown in Fig. 12 that the pipe-shaped volume defects appeared also in the middle part of the crystal. It seems to be highly probable that the formation of the volume defects is connected with a strong perturbation of the growth conditions, appearing as growth bands with high contrast. The volume defects appear to start a little bit earlier, but it is in consistence with the interpretation as solute trails. At the moment of perturbation, there was probably constitutional supercooling which triggered local solving of the material inside the already grown crystal. This perturbation is propagated during the next stages of growth of the crystal in a form of a pipe, where the melt crystallize a little later. The other large defect appearing in the middle part of the sample shown in Fig. 13 seems to be an irregularly bounded area of the facetted growth.

The important information concerning the observed volume defects received from the Berg-Barrett topograph shown in Fig. 13 was that the defects can be divided in two categories. In the case of the first one, as in the case of facets in the core, only the extinction contrast at boundaries of the defects becomes visible. It means that the volume of defects reflects X-rays like the rest of crystal. It may be concluded that the first category of the volume defects, similarly to the core contains $Y_3Al_5O_{12}$, probably differing with the concentration of dopant. The second category refers to the defects appearing in the Berg-Barrett topographs as more clear areas; here on the direct copies with black contrast. Most probably they do not reflect the radiation, but reflecting of some small intensity cannot be excluded.

The lack of diffraction may be probably explained by the presence of a different crystallographic phase or higher misorientation exceeding 20°. We tried to examine very carefully the first possibility. For that purpose we performed a number of investigations including the powder diffractometry of powdered material from initial parts of the crystals, X-ray microanalysis and micro Laue--method with beam collimated to 0.1 μm. Careful optical microscopic examination did not reveal any inhomogene-

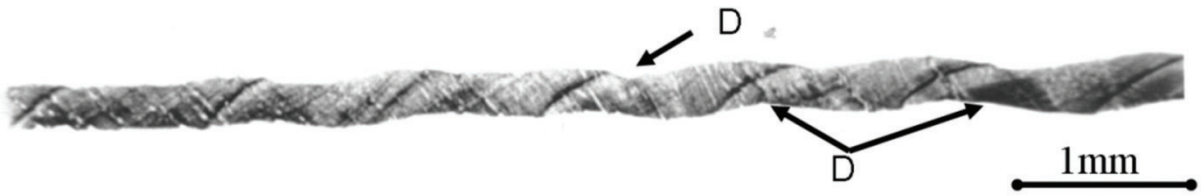

Fig. 14. Synchrotron radiation white beam transmission section topograph for the sample cut from $Ca_{0.5}Sr_{0.5}NdAlO_4$ single crystal, grown by the Czochralski method in $\overline{367}$ reflection, $\lambda = 0.047$ nm, $\mu t = 2.3$; D denotes characteristic kinks of the section topograph which may indicate the deformation of the crystal lattice – according to A. Malinowska et al. [61].
Rys. 14. Synchrotronowy transmisyjny przekrojowy topogram w wiązce białej próbki wyciętej z monokryształu $Ca_{0.5}Sr_{0.5}NdAlO_4$ otrzymanego metodą Czochralskiego; refleks $\overline{367}$, $\lambda = 0{,}047$ nm, $\mu t = 2{,}3$; D – charakterystyczne stopnie topogramu przekrojowego wskazujące na deformację sieci krystalicznej. Na podstawie A. Malinowska i in. [61].

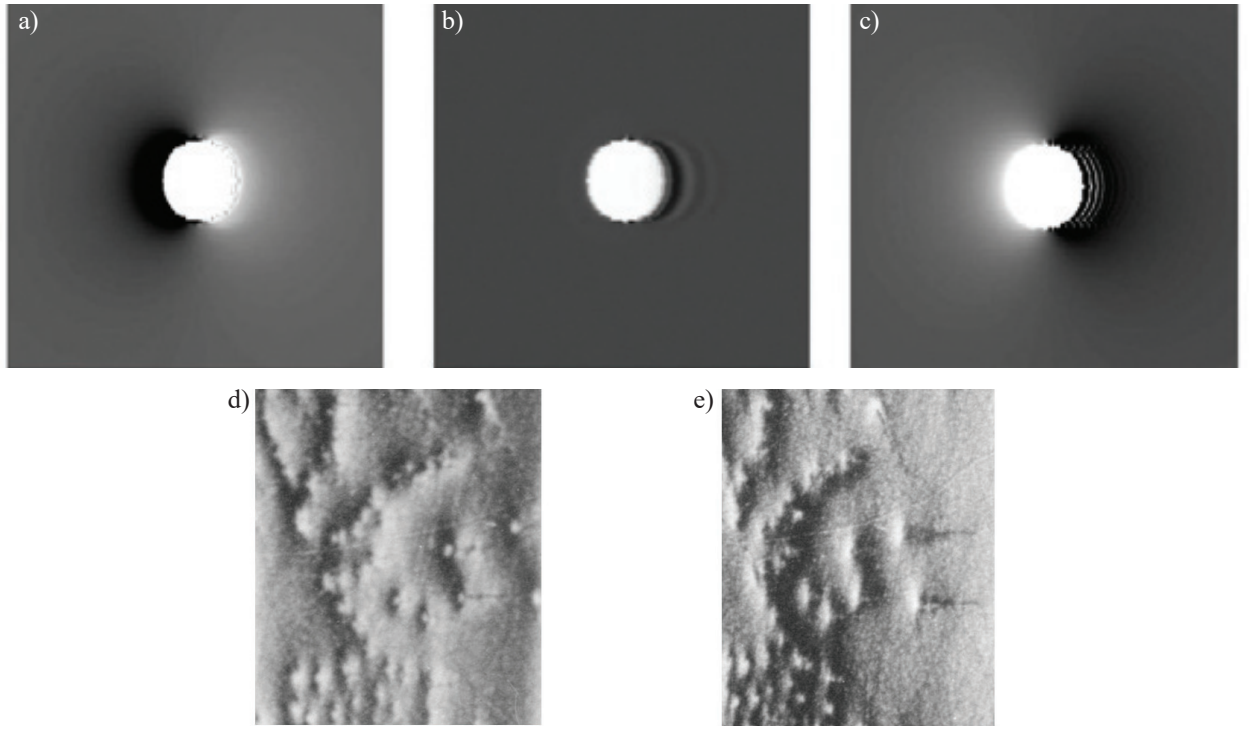

Fig. 15. (a)-(c) Simulated monochromatic beam X-ray topographic images of shrinking rod-like inclusions of 150 μm in diameter for angular setting respectively at low angle flank, maximum and high angle flank of the rocking curve, taken in 008 reflection of 0.1115 nm radiation.(d), (e) monochromatic beam X-ray topographs of volume inclusions in $SrLaGaO_4$ (SLG) crystals exhibiting some features of rod-like inclusions respectively for low and high angle flank of the rocking curve. The contrast of the defects is reversed for the two flanks. According to W. Wierzchowski et al. [57].
Rys. 15. (a) – (c) Symulowane topogramy (dla wiązki monochromatycznej) walcowatego wtrącenia o charakterze ściągającym sieć i średnicy 150 μm; topogram zasymulowany dla trzech różnych ustawień kątowych: na lewym (niskokątowym) zboczu krzywej odbić (a), w maksimum krzywej odbić (b) oraz na prawym (wysokokątowym) zboczu krzywej odbić (c); refleks 008, promieniowanie 0,1115 nm. (d), (e) rentgenowskie dyfrakcyjne topogramy w wiązce monochromatycznej objętościowych wtrąceń w krysztale $SrLaGaO_4$ (SLG) wykazujące cechy walcowych wydzieleni z punktów (a) – (c) odpowiednio dla nisko- i wysokokątowego zbocza krzywej odbić. Widoczne odwrócenie kontrastu dyfrakcyjnego dla obu zboczy krzywej odbić. Na podstawie W. Wierzchowski i in. [57].

ities suggesting the presence of another crystallographic phase. Powder diffractometry did not reveal any peaks apart from those of $Y_3Al_5O_{12}$. It may also be concluded as an important result, because the volume concentration of unreflecting defects evaluated from the ratio of their area to the surface of the sample seem to be greater than 5%, exceeding the sensitivity of the powder diffractometry. X-ray microanalysis did not reveal any detectable change in the concentration of yttrium or aluminium, but an increase of niobium concentration was observed in both kinds of volume defects and in the core. Both transmission and back-reflection micro-Laue investigation of the nonreflecting volume defects with conventional radiation did not reveal any traces of additional pattern [56].

The synchrotron investigation can reveal significant strains associated with the segregation fringes [61]. In particular they can be revealed in the transmission and reflection section topography. Characteristic results were obtained for $Ca_{0.5}Sr_{0.5}NdAlO_4$ single crystal grown by the Czochralski method in the [100] direction. The crystal

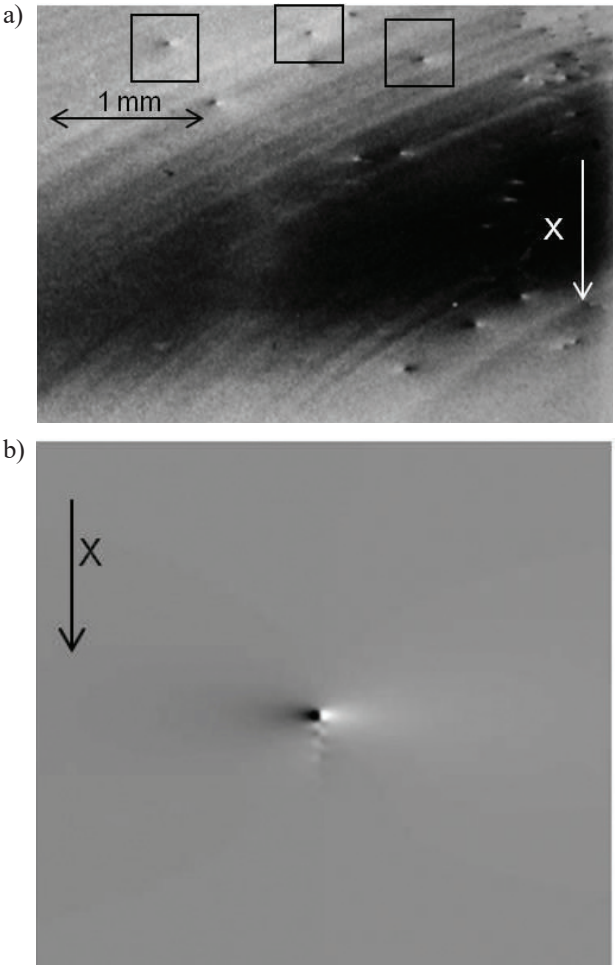

Fig. 16. (a) Monochromatic beam topographic images of dislocation outcrops in the sample cut out from $Y_3Al_5O_{12}$ (YAG); 444 reflection, 0.1115 nm radiation; (b) simulated topographic image of the dislocation outcrop corresponding to the areas limited by squares in (a). According to K. Mazur et al. [70].

Rys. 16. (a) Rentgenowski dyfrakcyjny topogram w wiązce monochromatycznej ujść dyslokacji w próbce wyciętej z monokryształu $Y_3Al_5O_{12}$ (YAG); refleks 444, promieniowanie 0,1115 nm; (b) Symulowany topogram (dla wiązki monochromatycznej) ujścia dyslokacji odpowiadający obszarowi zaznaczonemu przez kwadrat na Rys. (a).Według K. Mazur i in. [70].

seems to be very interesting in the view of its very high lattice parameter changes and strains connected with the composition changes and the presence of large amount of volume defects interpreted as the solute trails. The representative section topograph is shown in Fig.14 [61].

The identification of the solute trails in garnets and $SrLaGaO_4$ (SLG) crystals was confirmed using the simulation based on numerical integration of the Takagi-Taupin equations. The simulation was performed with a model that enabled realistic simulations of the monochromatic beam topographic images of some solute trails in garnets and the Bragg-case section images of some defects resembling rod-like inclusions described in [73]. The approximation of the strain field of rod–like dislocations was obtained by a summation of the contributions from the point-like inclusions used the formulae derived from those given by Sen [77].

The example of the simulations confirming the expected presence of rod like inclusions in the case of SLG crystals is presented in Fig. 15. The simulation corresponds to an assumed shrinkage type inclusion at the angular setting for low angle flank maximum and a large angle flank respectively.

As the reference in Fig. 16 we quote the experimental and numerically simulated images of dislocations outcrops in YAG substrates according to [70].

Representative synchrotron and conventional topographs of the samples cut out from $(Ca_{0.28}Ba_{0.72})_y(Sr_{0.61}Ba_{0.39})_{1-y}Nb_2O_6$ (CSBN) crystals are shown in Figs. 17 - 18. Contrary to $Sr_xBa_{1-x}Nb_2O_6$ (SBN) and $Ca_xBa_{1-x}Nb_2O_6$ (CBN) crystals we did not observe any glide bands in the CSBN [74]. The most characteristic defects were segregation fringes (marked by *S* and *G*) and dislocations or some rod-like inclusions (marked by *D*) around the core present in the central part of the samples.

The topographs revealed a very characteristic phenomenon, which consisted in the presence of two different sys-

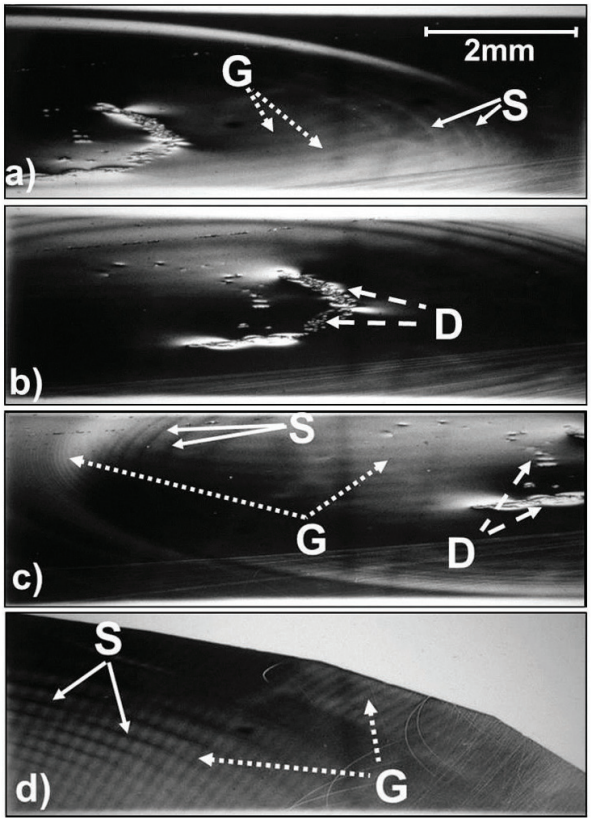

Fig. 17. (a) - (d) Synchrotron monochromatic beam topographs $(Ca_{0.28}Ba_{0.72})_y(Sr_{0.61}Ba_{0.39})_{1-y}Nb_2O_6$ (CSBN) in 004 reflection of 0.1115 nm radiation. According to W. Wierzchowski et al. [74].

Rys. 17. (a) - (d) Synchrotronowe topogramy rentgenowskie w wiązce monochromatycznej monokryształu $(Ca_{0.28}Ba_{0.72})_y(Sr_{0.61}Ba_{0.39})_{1-y}Nb_2O_6$ (CSBN); refleks 004, promieniowanie 0.1115 nm. Na podstawie W. Wierzchowski i in. [74].

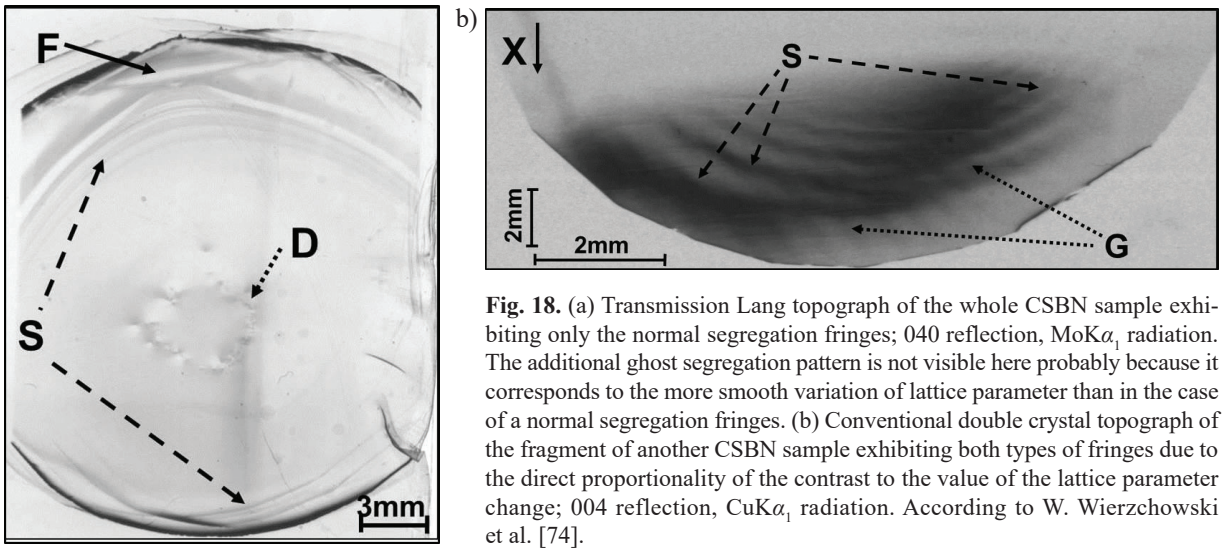

Fig. 18. (a) Transmission Lang topograph of the whole CSBN sample exhibiting only the normal segregation fringes; 040 reflection, MoKα_1 radiation. The additional ghost segregation pattern is not visible here probably because it corresponds to the more smooth variation of lattice parameter than in the case of a normal segregation fringes. (b) Conventional double crystal topograph of the fragment of another CSBN sample exhibiting both types of fringes due to the direct proportionality of the contrast to the value of the lattice parameter change; 004 reflection, CuKα_1 radiation. According to W. Wierzchowski et al. [74].

Rys. 18. (a) Transmisyjny topogram Langa całej próbki wyciętej z monokryształu CSBN ujawniający jedynie zwykłe prążki segregacyjne; refleks 040, promieniowanie MoKα_1. Brak widocznych *ghost segregation pattern* spowodowane jest łagodniejszymi wahaniami parametru sieciowego niż w przypadku zwykłych prążków segregacyjnych; (b) Konwencjonalny topogram dwukrystaliczny fragmentu innej próbki CSBN ujawniający oba rodzaje prążków segregacyjnych dzięki silniejszej zależności kontrastu od nawet małych zmian parametru sieciowego; refleks 004, promieniowanie CuKα_1. Według W. Wierzchowski i in. [74].

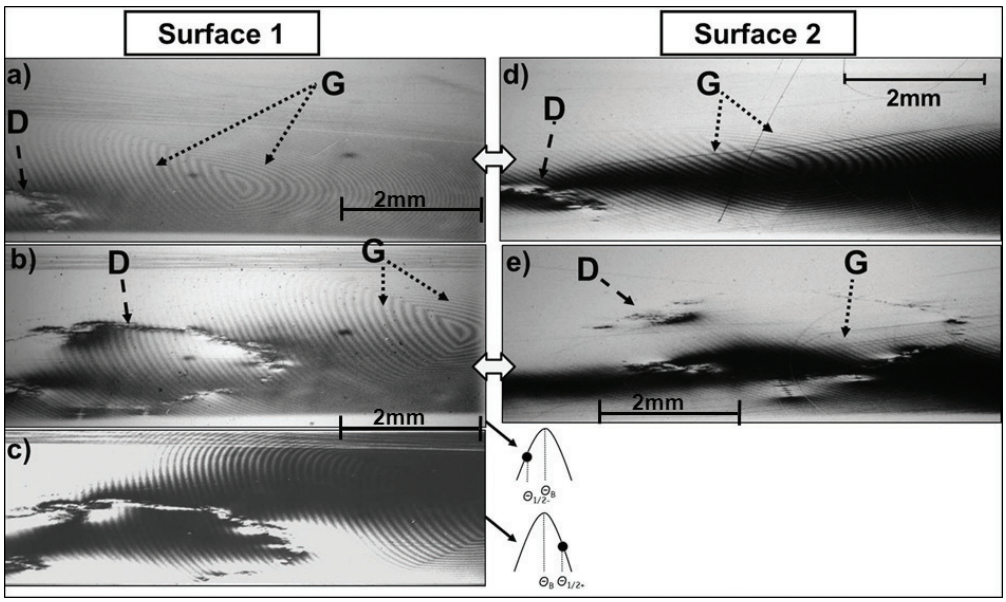

Fig. 19. Synchrotron monochromatic beam back-reflection projection topographs for two surfaces of the (001)-oriented sample cut out from the near-end part of the $(Ca_{0.28}Ba_{0.72})_{0.75}(Sr_{0.61}Ba_{0.39})_{0.25}Nb_2O_6$ (CSBN-75) crystal: (a) - (c) - front surface and (d), (e) - rear surface respectively; (a) shows a characteristic three sector pattern of *ghost* fringes seen also on the other side of the crystal (d); (b), (c) were taken from the middle region of the sample for two flanks of the rocking curve showing the inversion of the contrast of the *ghost* pattern fringes. The middle region of the sample on the other surface is shown in (e); 002 reflection, 0.1115 nm radiation. The width at half maximum of the rocking curve was close to 8.5 arc sec., S - *normal* segregation fringes, G - *ghost* segregation pattern, D - diffraction contrasts corresponding to the defects in the core region. According to W. Wierzchowski et al. [74].

Rys. 19. Synchrotronowe rentgenowskie odbiciowe topogramy projekcyjne w wiązce monochromatycznej dla dwóch powierzchni próbki o orientacji (001) wyciętej z końcowej części monokryształu $(Ca_{0.28}Ba_{0.72})_{0.75}(Sr_{0.61}Ba_{0.39})_{0.25}Nb_2O_6$ (CSBN-75). (a) - (c) - przednia powierzchnia (d), (e) - odpowiednio tylna powierzchnia (a) pokazuje charakterystyczny trójsektorowy układ prążków *ghost fringes*, widoczny również na przeciwnej stronie próbki. (d); topogramy (b), (c) naświetlone w środkowym obszarze próbki dla dwu przeciwnych zboczy krzywej odbicia wykazują odwrócenie się kontrastu prążków *ghost*. Środkowy obszar przeciwnej powierzchni próbki pokazano na topogramie (e); Wszystkie topogramy naświetlano w refleksie 002, dla promieniowania 0,1115 nm. Szerokość połówkowa maksimum krzywej odbicia wynosiła około 8,5 sekund kątowych, Przez S - oznaczono normalne prążki segregacyjne, natomiast przez G - prążki segregacyjne *ghost*, D - oznacza kontrast pochodzący od defektów w obszarze rdzenia. Według W. Wierzchowski i in. [74].

tems of segregation fringes forming a crossing pattern [74]. One of the systems (marked by *S* in Figs. 17 - 18) is connected with the subsequent position of the growth surface being coaxial with the core and the boundaries of the crystal. The second system the so called *ghost* segregation pattern, marked by G in Figs. 17 - 19, crossing the previous one, cannot be connected with the position of the growth surface. In addition, investigation of the relatively thick crystal wafers (Fig. 19) confirmed that this fringe system is changing relatively slowly; hence it can propagate through large distances along the growth axis.

The inversion of the diffraction contrast in the monochromatic beam synchrotron topographs from white to black for opposite flanks of the rocking curve (Figs. 19b, c) indicates that the observed contrast of segregation fringes is caused by the slight crystal lattice parameters fluctuations.

Neither scanning electron microscopic investigations nor X-ray microanalysis (with the accuracy 0.5 - 1.0 at. %) revealed any fluctuations of composition corresponding to the systems of segregation fringes.

The possible explanation of the observed phenomenon is a kind of *ghost* segregation pattern reproducing some chemical composition changes in the new part of the growing crystal [74]. The other possibility is connected with the formation of a kind of relief on the growth surface, which was connected with former segregation effects and remained after the change of the growth surface. It is worth to notice that the *ghost* segregation fringes were effectively revealed only by means of the synchrotron monochromatic beam topography and conventional double crystal topography, but were not visible in the transmission Lang topography. This may results from the contrast formation mechanism in the first two methods, where the contrast depends only on the relative lattice parameter changes on the level of 10^{-6}. Contrary to that the Lang topography reveals the segregation fringes thanks to the lattice parameters gradients, which may not be large enough in the *ghost* segregation fringes, where one can expect a significant smoothening in course of propagation of the effect along the crystal. The Lang topograph shown in Fig. 18 reproduced the near-edge part of the crystal containing some faceted growth region (marked by F) similar to the one discussed in [66].

5. Conclusions

Conventional methods of X-ray diffraction topography have been successfully used in many papers describing the growth and the defect structure in oxide crystals grown with various methods especially with the Czochralski method. The possibility of X-ray diffraction topography was significantly increased by the use of synchrotron radiation offering a better resolution and collimation of the beam as well as the possibility of using more suitable radiation wavelengths. For this reason the synchrotron radiation topography has also been widely used for the investigation of the defect structure of many crystals particularly the oxide crystals.

In the present paper the possibilities of the conventional and synchrotron diffraction topography have been illustrated on the basis of the results obtained by the authors. The paper includes the investigation of the recently developed crystals as well as examples quoted from the previous publications illustrating the studies of the defects characteristic for the oxide crystals in particular the examples of studies of segregation fringes, mosaic structures and solute trails shown together with some applications of the numerical simulations of the defect structure based on the numerical integration of the Takagi-Taupin equations. We also included topographs illustrating the new phenomenon of the simultaneous existence of the two types of segregation fringes called by us the ghost segregation pattern most probably caused by the transmission of some chemical composition changes in the growing crystal.

Acknowledgements

The authors would like to express their great thanks to dr. Carsten Paulmann for his cotribution to the paper, especially the technical assistance in the majority of the presented investigation. They would also to thank for the experimental help and for many useful scientific remarks.

References

[1] Solski I. M., Sugar Yu D., Vakiv M. M.: Growing Large Size Complex Oxide Single Crystals by Czochralski Technique for Electronic Devices, *Acta Phys. Pol. A*, 2013, 124, 314 – 320

[2] Bruni F. J., Johnston G. M.: Careful system design speeds laser-crystal growth, *Solid State Laser Materials Laser Focus World*, 1994, 205 – 212

[3] Cockayne B., Gates M. P.: Growth striations in vertically pulled oxide and fluoride single crystals, *J. Mat. Science*, 1967, 2, 118 – 123

[4] Carruthers J. R.: Origins of convective temperature oscillations in crystal growth melts, *J. Cryst. Growth*, 1976, 32, 13 – 26

[5] Dąbkowska H. A., Gaulin B. D.: Growth of single crystals of selected cup rates by the optical floating zone technique, *Journal of Optical Electronics and Advanced Materials*, 2007, 9, 1215 – 1220

[6] Dąbkowska H. A., Dabkowski A. B.: Crystal Growth of Oxides by optical Floating Zone, in Springer Handbook of Crystal Growth, Springer, 2010

[7] Brown C. S., Kell R. C., Thomas L. A., Wooster N., Wooster W. A.: The growth and properties of

large crystals of synthetic quartz, *Mineralogical Magazine*, 1952, 29, 858 – 874

[8] Brown C. S., Thomas L. A.: The effect of impurities on the growth of synthetic quartz, *J. Phys. Chem. Sol.*, 1980, 13, 337 – 343

[9] Li W. - J., Shi E. - W., Zhong W. - Z., Yin Z. - W.: Growth mechanism and growth habit of oxide crystals, *J. Cryst. Growth*, 1999, 203, 86 – 196

[10] Zhang S., Yao S., Li J., Zhao L., Wang J., Boughton R. I.: Growth habit control of ZnO single crystals in molten hydrous alkali solutions, *J. Cryst. Growth*, 2011, 336, 56 – 59

[11] McLaren A. C., Cook R. F., Hyde S. T., Tobin R. C.: The mechanisms of the formation and growth of water bubbles and associated dislocation loops in synthetic quartz, *Phys. Chem. Minerals*, 1983, 9, 79 – 94

[12] Tanner B. K.: X-ray diffraction Topography, Pergamon Press, Oxford, 1976

[13] Bowen D. K., Tanner B. K.: High resolution X-ray diffractometry and topography, Taylor and Francis, London, 1998

[14] Authier A.: Dynamical theory of X-ray diffraction, Oxford University Press, Oxford, 2001

[15] Lang A. R.: A method for the examination of crystal sections using penetrating characteristic radiation, *Acta. Metall.*, 1957, 5, 358 – 364.

[16] Lang A. R.: Direct observation of Individual Dislocation by X-Ray Diffraction, *J. Appl. Phys.*, 1958, 29, 597 – 598

[17] Bonse U., Kappler E.,: Röntgenographisches Abbildung des Verzerrungsfeldes einzelner Versetzungen in Germanium-Einkristallen, *Z. Naturforsch*., 1958, 214, 348 – 349

[18] Bond W. L., Andrus J.: Structural Imperfections in Quartz Crystals, *Am. Minneralogist*, 1952, 37, 622 – 632

[19] Bonse U.: Zur röntgenographishen Bestimmung des Types einzelner Versetzungen in Germanium--Einkristallen, *Z. Phys*, 1958, 153, 278 – 296

[20] Renninger M.: The Asymmetric Bragg Reflection and its Application in Double Diffractometry, *Adv. X-ray Analysis*, 1967, 10, 32 – 36

[21] Renninger M., Doppel diffraktometrische Transmissions-Topographie, *Z. Naturforsch. (a)*, 1964, 19, 783 – 787

[22] Schultz L. G.: Method of using a fine-focus X-ray tube for examining the surface of a single crystal, *Trans. AIME*, 1954, 200, 1082 – 1083

[23] Berg W. F.: Übereinröntgenographische Methode zur Untersuchung von Gitterstörungen an Kristallen, *Naturwissenschaften*, 1931, 19, 391 – 396

[24] Barrett C. S.: A new microscopy and its potentialities, *Trans. Metal. Soc*. AIME, 1945, 161, 15 – 64

[25] Tuomi T., Naukkarinen K., Rabe P.: Use of Synchrotron X-Ray Diffraction Topography, *Phys. Stat. Sol. (a)*, 1974, 25, 93 – 106

[26] Hart M.: Synchrotron radiation - its application to high-speed, high-resolution X-ray diffraction topography, *J. Appl. Cryst.*, 1975, 8, 436 – 444

[27] Tanner B. K., Safa M., Midgley D., Bordas J.: Observation of magnetic domain wall movements by X-ray topography using synchrotron radiation, *J. of Magnetism and Magnetic Materials*, 1976, 1, 337 – 341

[28] Tanner B. K.: Crystal assessment by X-ray topography using synchrotron radiation, *Progress in Crystal Growth and Characterization,* 1976, 1, 23 – 56

[29] Hart M., Sauvage M., Siddons D. P.: White beam synchrotron X-ray interferometry, *Acta Cryst. A*, 1980, 36, 947 – 951

[30] Wheatmore R. W., Goddard P. A., Tanner B. K.: Direct imaging of travelling Rayleigh waves by stroboscopic X-ray topography, *Nature*, 1982, 299, 44 – 46

[31] High-throughput, High-resolution X-ray topography imaging system: XRT micron, *The Rigaku Journal,* 2014, 30, 1

[32] Omote K.: Crystal defects in SiC wafers and a new X-ray topography system, *The Rigaku Journal*, 2013, 29, 1–8

[33] Lang A. R., Miuscov V.F.: Dislocation configurations in magnesium oxide observed by x-ray topography, *Phil. Mag.*, 1964, 10, 263 – 268

[34] Basterfield J., Prescott M. J., Cockayne B.: An X-ray diffraction topographic study of single crystals of melt-grown yttrium aluminium garnet, *J. Material Sci*., 1968, 3, 33 – 40

[35] Cockayne B., Chesswas M., Born P. J., Filby J. D.: The morphology and defect characteristics of vertically pulled $MgAl_2O_4$ single crystals, *J. Material Sci.*, 1969, 4, 236 – 241

[36] Mag C. A., Shah J. S.: Dislocation reactions and cavitation studies in melt-grown sapphire, *J. Mater. Sci.*, 1969, 4, 179 – 187

[37] Belouet C.:About the crystalline perfection of Nd--doped YAG single crystals, J. Cryst. Growth, 1972, 15, 188 – 194

[38] Neuroth G., Wallrafen F.: Czochralski growth and characterization of pure and doped $YAlO_3$single crystals, *J. Cryst. Growth,* 1999, 435 – 439

[39] Stacy W. T., Enz U.: The characterization of magnetic bubble-domain materials with X-ray topography, *Trans IEEE Magnetics Mag*., 1972, 8, 268 – 272

[40] Stacy W. T.: Dislocations, facet regions and growth striations in garnet substrates and layers, *J. Cryst. Growth*, 1974, 24/25, 137 – 143

[41] Spencer W. J., Haruta K.: Defects in Synthetic Quartz, *J. Appl. Phys.*, 1966, 37, 549 – 554

[42] McLaren A. C., Osborne C. F., Saunders L. A.: X--ray topographic study of dislocations in synthetic quartz, *Phys. Stat. Sol. (a)*, 1971, 4, 235 – 247

[43] Takagi M., Mineo H., Sato M.: Defects in synthetic quartz, *J. Cryst. Growth*, 1974, 24/25, 541 – 543

[44] Croxall D. F., Ward R. C. C., Wallace C. A., Kell

R. C.: Hydrothermal growth and investigation of Li-doped zinc oxide crystals of high purity and perfection, *J. Cryst. Growth*, 1974, 22, 117 – 124

[45] Baruchel J., Di Michiel M., Lafford T., Lhuissier P., Meyssonier J., Nguyen-Thi H., Philip A., Pernot P., Salvo L., Scheel M.: Synchrotron X-ray imaging for crystal growth studies, *C. R. Physique*, 2013, 14 (1-2), 208 – 220

[46] Kasper E., Burle N., Escoubas S., Werner J., Oeheme M., Lyutovich K.: Strain relaxation of metastable SiGe/Si: Investigation with two complementary X-Ray Techniques, *J. Appl. Phys*., 2012, 111, 063507-1 – 063507-10.

[47] Yao S., Hu X., Yan T., Liu H., Wang J., Qin X., Chen Y.: Twinning structures in near-stoichiometric lithium niobate single crystals, *J. Appl. Cryst*., 2010, 43, 276 – 279

[48] Muehlberg M., Burianek M., Joschko B., Klimm D., Danilewsky A., Gelissen M., Bayarjargal L., Görler G. P., Hildmann B. O.: Phase equilibria, crystal growth and characterization of the novel ferroelectric tungsten bronzes $Ca_xBa_{1-x}Nb_2O_6$ (CBN) and $Ca_xSr_yBa_{1-x-y}Nb_2O_6$ (CSBN), *J. Cryst.Growth*, 2008, 310, 2288 – 2294

[49] Prokhorov I. A., Zakharov B. G., Senchekov A. S., Egorov A. V., Camel D., Tison P.: Structural features of Ge(Ga) single crystals grown by the floating zone method in microgravity, *J. Cryst. Growth*, 2008, 310 (22), 4701 – 4707

[50] Yoneda Y., Mizuki J., Takeda H., Shiosaki T.: X--ray topography of piezoelectric $La_3Ta_{14}Ga_{5.5}O_{14}$ crystal grown by Czochralski Method, *IEEE Trans. Ultrason. Ferroelectr. Freq. Control*, 2008, 55 (5), 971 – 974

[51] Yao G.D., Hou S.Y., Dudley M., Phillips J.M.: Synchrotron X-ray Topography Studies of Twin Configurations in Lanthanum Aluminate Single Crystals, *J. Mater. Res*., 1992, 7, 1847 – 1855

[52] Dudley M., Yao G. D.: Synchrotron Topography of Phase Transitions in Perovskite-Like Crystals, *J. Phys. D*, 1993, 26, A120 – A125

[53] Cerva H., Graeff W.: Contrast investigations of surface acoustic waves by stroboscopic topography II Wave field deviation contrast, *Phys. Stat. Sol. (a)*, 1985, 87, 507 – 516

[54] Wieteska K.: X-ray topography using synchrotron radiation, *Acta Physica Polonica A*, 1994, 86, 545 – 552

[55] Malinowska A., Lefeld-Sosnowska M., Härtwig J.: Contrast in transmission X-ray diffraction topographs of growth defects in the core of $SrLaGaO_4$ single crystals, *J. Appl. Cryst.*, 2013, 46, 48 – 54

[56] Mazur K., Wierzchowski W.: X-ray topographic investigation of growth defects and lattice parameter measurements within crystals of heavily neodymium doped yttrium aluminium garnet, *J. Cryst. Growth*, 1995, 148, 345 – 354

[57] Wierzchowski W., Wieteska K., Malinowska A., Wierzbicka E., Lefeld-Sosnowska M., Świrkowicz M., Łukasiewicz T., Pajączkowska A., Paulmann C.: Synchrotron Diffraction Topography in Studying of the Defect Structure in Crystals Grown by the Czochralski Method, *Acta Phys. Pol. A*, 2013, 124, 350 – 356

[58] Wieteska K., Wierzchowski W., Wierzbicka E., Malinowska A., Lefeld-Sosnowska M., Łukasiewicz T., Graeff W.: X-ray topographic studies of defects structure in YVO_4 crystal, *Acta Phys. Pol. A*, 2008, 114 (2), 455 – 461

[59] Wierzbicka E., Malinowska A., Wieteska K., Wierzchowski W., Lefeld-Sosnowska M., Świrkowicz M., Łukasiewicz T., Paulamann C.: Characterization of the Defect Structure in Gadolinum Orthovanadate Single Crystals Grown by the Czochralski Method, *Acta Phys. Pol. A*, 2012, 121, 906 – 909

[60] Wieteska K., Wierzchowski W., Graeff W., Lefeld--Sosnowska M., Pajączkowska A., Wierzbicka E., Malinowska A.: Investigation of the defect distribution along the growth direction in GdCOB crystals by synchrotron and conventional X-ray topography, *J. Aloys. Comp.*, 2005, 401, 69 – 74

[61] Malinowska A., Lefeld-Sosnowska M., Wieteska K., Wierzchowski W., Graeff W., Pajaczkowska A.: X-ray topography of $Ca_{0.5}Sr_{0.5}NdAlO_4$ single crystal, *J. Cryst. Growth*, 2008, 310 (14), 3398 – 3402

[62] Lefeld-Sosnowska M., Olszyńska E., Wierzchowski W., Wieteska K., Graeff W., Pajączkowska A., Kłos A.: Conventional and synchrotron radiation back reflection topography of $GdCa_4O(BO_3)_3$ crystals, *J. Alloys. Comp.*, 2004, 382, 153 – 159

[63] Wieteska K., Wierzchowski W., Malinowska A., Turczyński S., Lefeld-Sosnowska M., Pawlak D.A., Łukasiewicz T., Paulmann C.: Synchrotron Topographic Studies of Domain Structure in Czochralski Grown $Pr_xLa_{1-x}AlO_3$ and $Pr_xLa_{1-x-y}Mg_yAlO_3$ Crystals, *Acta Phys. Pol. A*, 2012, 121, 910 – 914

[64] Wieteska K., Wierzchowski W., Malinowska A., Turczyński S., Lefeld-Sosnowska M., Pawlak D. A., Łukasiewicz T., Graeff W.: X-ray Topographic Investigations of Domain Structure in Czochralski Grown $Pr_xLa_{1-x}AlO_3$ Crystals, *Acta Phys. Pol. A*, 2010, 117, 268 – 271

[65] Wieteska K., Wierzchowski W., Malinowska A., Lefeld-Sosnowska M., Świrkowicz M., Łukasiewicz T., Paulmann C.: Synchrotron diffraction topography of $Sr_xBa_{1-x}Nb_2O_6$ (SBN), $Ca_xBa_{1-x}Nb_2O_6$ (CBN) and mixed $(Ca_{0.28}Ba_{0.72})_y(Sr_{0.61}Ba_{0.39})_{1-y}Nb_2O_6$ (CSBN) crystals, *Rad. Phys. Chem.*, 2013, 93, 87 – 91.

[66] Kołodziejak K., Wierzchowski W., Wieteska K., Malinowski M., Graeff W., Łukasiewicz T.: The Investigation of structural perfection and faceting in highly Er-doped $Yb_3Al_5O_{12}$ Crystals, *Cryst. Res. Technol*., 2008, 43, 369 – 373

[67] Wierzchowski W., Wieteska K., Graeff W., Sakowska H., Łukasiewicz T., Pawłowska M.: Synchrotron X-ray investigation of $La_{0.3}Sr_{0.7}Al_{0.65}Ta_{0.35}O_3$ crystals, *Cryst. Res. Technol*. 2005, 40, 517 – 522

[68] Savytskii D., Senyshyn A., Matkowskii A., Vaylech-

ko L., Wieteska K., Wierzchowski W., Łukasiewicz T., Bismayer U.: White beam synchrotron X-ray topography studies of twinning in $GdFeO_3$-type perovskite crystals, *Z. Kristallogr.*, 2003, 218, 17 – 25

[69] Malinowska A., Lefeld-Sosnowska M., Wieteska K., Wierzchowski W., Härtwig J., Graeff W.: Synchrotron topographic studies of growth defects in the core of a $SrLaGaO_4$ crystals, *Phys. Stat. Sol. (a)*, 2009, 206, 1816 – 1819

[70] Mazur K., Sarnecki J., Wierzchowski W., Wieteska K., Turos A.: X-ray characterization of GGG homoepitaxial layers with introduced divalent Ni ions, *Rad. Phys. Chem*., 2011, 80, 1084 – 1087

[71] Mazur K., Sarnecki J., Borysiuk J., Wierzchowski W., Wieteska K., Turos A.: X-ray study of gadolinium gallium garnet epitaxial layers containing divalent Co ions, *Thin Solid Films*, 2011, 519, 2111 – 2115

[72] Paszkowicz W., Romanowski P., Bąk-Misiuk J., Wierzchowski W., Wieteska K., Graeff W., Iwanowski R.J., Heionnen M.H., Ermakova O., Dąbkowska H.A.: Characterization of an Yb:$LuVO_4$ single crystal using X-ray topography, high-resolution X-ray diffraction, and X-ray photoelectron spectroscopy, *Rad .Phys. Chem.*, 2011, 80, 1001 – 1007

[73] Balcer T., Wierzchowski W., Wieteska K.: The Simulation of Bragg-Case Section Images of Dislocations and Inclusions in Aspect of Identification of Defects in SiC Crystals, *Acta Phys. Pol. A*, 2010, 117, 336 – 340

[74] Wierzchowski W., Wieteska K., Malinowska A., Wierzbicka E., Romaniec M., Lefeld-Sosnowska M., Świrkowicz M., Łukasiewicz T., Sakowska H., Paulmann C.: *Ghost* segregation pattern and ferroelectric domains in mixed calcium-strontium barium niobates, *X-ray Spectrometry*, 2015, 44, 356 – 362

[75] Wierzbicka E., Malinowska A., Wieteska K., Wierzchowski W., Lefeld-Sosnowska M., Świrkowicz M., Łukasiewicz T., Paulmann C.: Characterization of crystal lattice defects in calcium molybdate single crystals ($CaMoO_4$) by means of X-ray diffraction topography, X-ray Spectrometry, 2015, 44, 351 – 355

[76] Authier A.: Contrast of dislocation images in X-ray transmission topography, *Advan. X-ray Analysis*, 1967, 10, 9 – 31

[77] Sen B.: Note on the stresses produced by nuclei of thermo-elastic strain in a semi-infinite elastic solid, *J. Quant. Mech*, 1949, VIII (4), 365 – 369

[78] http://www.esrf.eu/home/UsersAndScience/Experiments/StructMaterials/ID19/Techniques/Diffraction/Overview.html (online 2018)

[79] Wierzbicka E., Malinowska A., Wierzchowski W., Kisielewski J., Świrkowicz M., Szyrski W., Romaniec M., Mazur K.: Rentgenowska topografia dyfrakcyjna defektów sieci krystalicznej w monokryształach $MgAl_2O_4$ i $ScAlMgO_4$ otrzymywanych w różnych warunkach technologicznych, *Materiały Elektroniczne (Electronic Materials)*, 2015, 43, 1, 29 – 39

[80] Malinowska A., Wierzbicka E., Wierzchowski W., Mazur K., Romaniec M., Kisielewski J., Świrkowicz M., Szyrski W., Drozdowski W.: Badanie struktury defektowej w nowych rodzajach scyntylacyjnych monokryształów mieszanych granatów lutetowo-itrowo-glinowych $[Lu_xY_{1-x}]_3Al_5O_{12}$ (LuYAG) niedomieszkowanych oraz aktywowanych prazeodymem, *Materiały Elektroniczne (Electronic Materials)*, 2015, 43, 1, 11 – 28

[81] Świrkowicz M., Szyrski W., Kisielewski J., Wieteska K., Wierzchowski W., Malinowska A., Wierzbicka E., Karaś A., Jurkiewicz-Wegner E.: Wzrost monokryształów molibdenianu wapnia domieszkowanych jonami ziem rzadkich ($CaMoO_4$:RE) do badań w zakresie immobilizacji odpadów radioaktywnych, *Materiały Elektroniczne (Electronic Materials)*, 2013, 41, 4, 10 – 19

LIST OF REVIEWERS 2016

dr inż. Mikołaj Baszun
dr hab. inż Tomasz Chmielewski
dr hab. Piotr Dłużewski
dr Jarosław Domagała
prof. dr hab. inż. Jerzy Filipiak
prof. dr hab. inż. Krzysztof Haberko
dr Jürgen Härtwig
prof. dr hab. inż. Ryszard Jachowicz
dr Benedykt Jany
dr inż. Marek Kostecki
dr hab. Grzegorz Kowalski
dr inż. Łukasz Kurpaska
prof. dr hab. inż. Bogusław Kusz
dr hab. inż. Ewa Markiewicz
dr Wojciech Maziarz
prof. dr hab. inż. Andrzej Milewski
dr Szymon Nosewicz
prof. dr hab. inż. Andrzej Olszyna
dr hab. Inż. Zbigniew Pędzich
dr hab. inż. Jerzy Potencki
prof. dr hab. Witold Ryba-Romanowski
dr Jerzy Sarnecki
prof. dr hab. inż. Mikołaj Szafran
prof. dr hab. Marian Surowiec

In memory

It is with great sadness that we have learned of the death of **Dr. Eng. Elżbieta Nossarzewska - Orłowska**, who passed away after a long and serious illness on November 30, 2016. Dr. Eng. Nossarzewska-Orłowska in the years 1972-2007 was the Head of the Department of Epitaxy at the Institute of Electronic Materials Technology (ITME) in Warsaw. She was an outstanding scientist and engineer in the field of silicon epitaxy for the applications in the semiconductor electronics; a co-author of patents and a prize winner of the state awards for the technical achievements. Thanks to her knowledge and a great involvement in the professional activity, the quality of silicon epitaxial layers produced in ITME gained a wide recognition among the manufacturers of the semiconductor devices not only in Europe but also in the USA, Japan and China.

Elżbieta Nossarzewska-Orłowska graduated from the Faculty of Chemistry at Warsaw University of Technology in 1959. Soon after graduation she started to work at the Industrial Electronics Institute, where she spent twelve years carrying out research on the preparation and properties of the luminescent materials. In 1972 she received her PhD degree in chemical sciences at the Institute of Physical Chemistry of Polish Academy of Sciences, the subject of her doctorate thesis being the mechanism and kinetics of cathodoluminescence. In the same year, she started to work as the Head of the Department of Epitaxy at the Semiconductor Materials Science and Production Center, which was later transformed into the Institute of Electronic Materials Technology. She held this position continuously for thirty five years.

Dr. Eng. Elżbieta Nossarzewska-Orłowska created scientific and organizational bases for the development of the silicon epitaxy technology to be applied in the domestic industry of the semiconductor devices which at that time applied the epiplanar technology. It was under her supervision, that over a hundred scientific and research projects were carried out in the field of silicon epitaxial layers, most of which ended with the practical implementation in the production of the epitaxial layers of new properties. The originality of many technological solutions was reflected in a dozen of patents for the manufacturing method of the silicon wafers with an epitaxial layer. Dr. Eng. Nossarzewska - Orłowska was also an author or a co-author of a number of scientific papers published both in Polish and international journals. To appreciate her merits in the development of the semiconductor industry in Poland, Dr. Eng. Elżbieta Nossarzewska - Orłowska was awarded numerous distinctions and national awards.

CEMAT-Silicon is definitely on the list of her great achievements. After the reconstruction of CEMAT'70 in 1989 it become an employee-owned company and took over the production of silicon single crystals. Her great involvement in the ongoing changes in the ownership of the company, helped to maintain high standards of the advanced technology of the silicon production for the semiconductor devices.

Working for ITME in the years 1993-1996, Dr. Eng. Nossarzewska-Orłowska, contributed also to the elaboration of a technology used in the production of porous silicon layers for the applications in the optoelectronic integrated circuits. In 1997, she initiated the studies on silicon single crystal resistance to radiation which started in ITME, and were conducted as a part of a wide international cooperation coordinated by CERN. The research was supervised by Dr. Eng. Nossarzewska-Orłowska until she retired in 2007. The investigations, carried out in a cooperation with the University of Hamburg, helped to further elaborate the technology of the epitaxial layers production for high energy particle detectors and develop new research methods that enabled to determine the properties of the radiational defects in silicon single crystals. The research conducted in the cooperation with CERN have been continued until today and its results have been highly valued by the international scientific community.

For us, who work for the Department of Epitaxy, Madam Elżbieta - as she was called - will remain in our memory as a person who had a great impact not only on our professional work but also on our personal life. She expected us to be deeply involved in our professional duties, but at the same time she was our friend who often helped us solve our private problems. The funeral of Madam Elżbieta took place on December 7, 2016. We paid our last tribute grieving her and her warm smile will always stay in our memory.

Colleagues from the Department of Epitaxy

INFORMATION FOR AUTHORS AND READERS

I. Submission rules

1. Only the manuscripts not published previously can be accepted. The author of the paper or the person submitting the manuscript of a multi-author work on behalf of all co-authors are required to declare that the work has not been published previously. If the test results contained in the manuscript have been presented earlier at a scientific conference or a symposium, the information on this fact should be given at the end of article containing the name, place and date of the conference. At the end of the article the authors should also provide the information on the sources of a financial support of the work, the contribution of scientific and research institutions, associations and other entities.
2. The manuscripts both in Polish and in English can be submitted. Due to introducing all the articles printed in *Electronic Materials* to the Internet , the author should make a statement on the copyright transfer of the author's economic rights to the Publisher.
3. Concerned about the reliability of the scientific work and the development of an ethical attitude of a researcher, a procedure has been introduced in order to prevent any cases of scientific dishonesty and unethical attitudes, defined as *ghostwriting* and *guest authorship* (*honorary authorship*):

- *ghostwriting* occurs when someone has made a substantial contribution to the publication without revealing his participation as one of the authors or without mentioning his role in the acknowledgments in the publication;
- *guest authorship* occurs when although the contribution of a given person is negligible or it has not taken place at all, he or she is an author/co-author of the publication.

The Editors require that the authors disclose the contributions of the individual authors in the preparation of a multi-author work, giving their affiliations and the information on their participation in the creative process, i.e. the information on the authors of the work's idea, assumptions, methods, etc. that have been utilized during the article preparation. The main responsibility for this information is borne by the author submitting the manuscript.
4. The Editors are obliged to keep the documentation of any forms of the scientific dishonesty, especially the violation of the ethical rules that are obligatory in science. All discovered cases of *ghostwriting* and "guest authorship" will be disclosed by the Editors, including the notification of the relevant entities, such as the institutions employing the authors, scientific societies, associations of scientific editors, etc.

II. Procedure of articles' review and approval for print

1. The author's materials directed for print in "Electronic Materials" are subjected to evaluation by the independent reviewers and the members of the Editorial Board.
2. The reviewers are suggested by the thematic editors – the members of the Editorial Board, responsible for a given subject field.
3. At least two independent reviewers from outside the research institution affiliated by the author of the publication are called for the evaluation of each publication.
4. In case of a publication in a foreign language, at least one reviewer is called, affiliated in a foreign institution with the seat in a country other than that of the origin of the author of the manuscript.
5. The author or authors of the manuscript and the reviewers do not know their identities (the so-called "double-blind review process").
6. A review is in written form and contains a clear conclusion of the reviewer concerning the article acceptance for the publication (without corrections or with necessary amendments to be made by the author) or its rejection.
7. The criteria for the article acceptance or rejection and a possible review form are disclosed to the public on the website of *Electronic Materials.*
8. The names of the reviewers of the individual publications or the editions are not disclosed. Once a year, in the last issue of "Electronic Materials", a list of the cooperating reviewers will be made public.
9. The Editors of *Electronic Materials* may edit the material obtained, shorten or supplement it (after an agreement with the author), or not qualify it for the publication.
10. The Editor-in-chief refuses to publish the authors' materials in the following cases:

- the contents of the manuscript are illicit,
- any signs of the scientific dishonesty, and especially *ghostwriting* and *guest authorship*, will be found out,
- the work has not received a positive final evaluation from the reviewers and the thematic editor.

11. The Editor-in-chief may refuse to publish the article if:

- the topic of the work is not in line with the subject field of *Electronic Materials*,
- the manuscript exceeds the acceptable volume and the author does not agree to shorten the article,
- the author refuses to make any necessary amendments proposed by the reviewer and the Editorial Board,
- the text or the illustrations provided by the author do not meet the technical requirements.